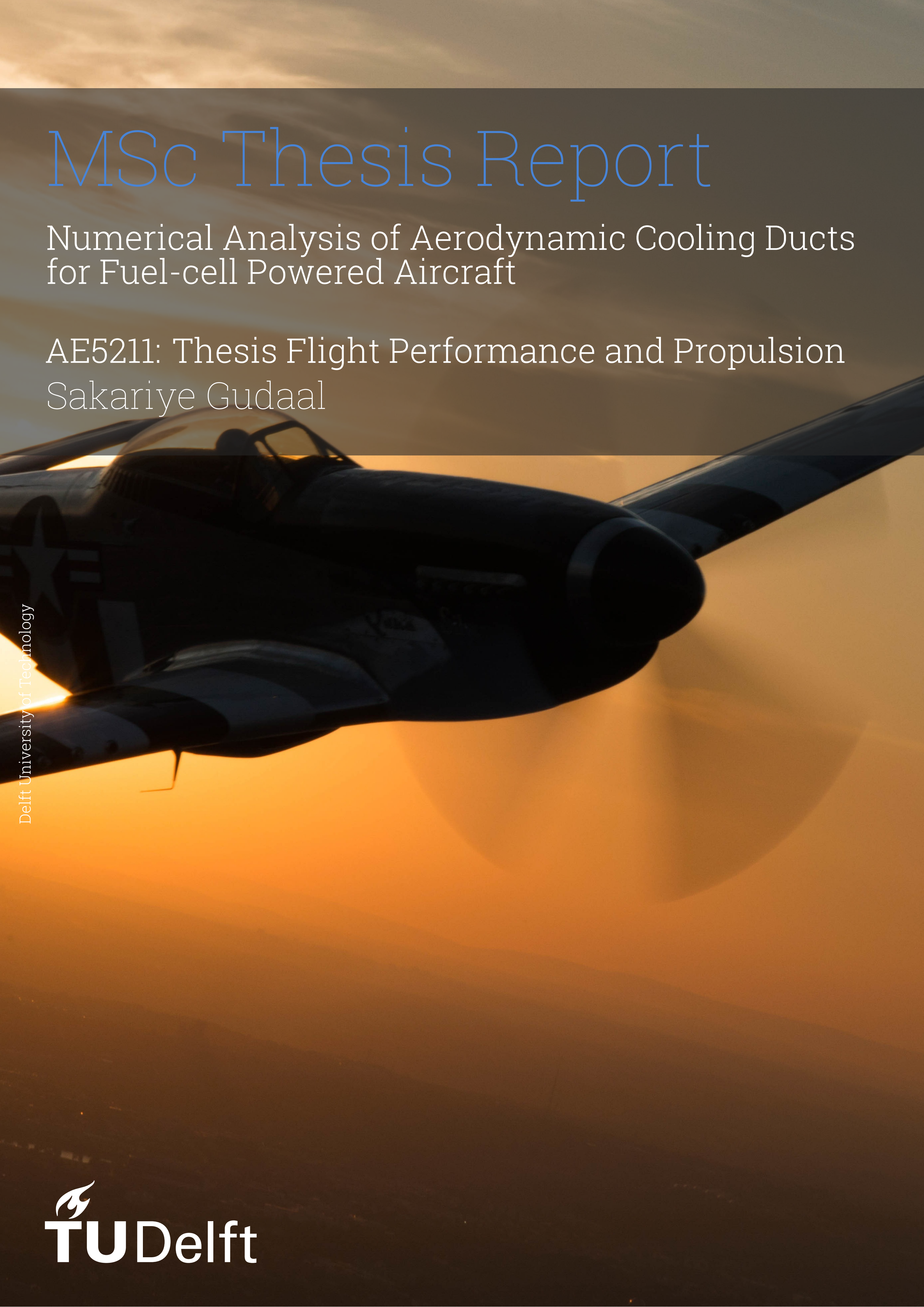

MSc Thesis Report

Numerical Analysis of Aerodynamic Cooling Ducts for Fuel-cell Powered Aircraft

AE5211: Thesis Flight Performance and Propulsion

Sakariye Gudaal

Delft University of Technology

TU Delft

MSc Thesis Report

Numerical Analysis of Aerodynamic Cooling Ducts for Fuel-cell Powered Aircraft

by

Sakariye Gudaal

to obtain the degree of Master of Science
at the Delft University of Technology,
to be defended publicly on Tuesday March 5, 2024 at 09:00 AM.

Student number:	4353196	
Thesis committee:	Prof. dr. ir. W. Baars,	TU Delft, supervisor
	Prof. dr. ir. M. Kotsonis,	TU Delft, supervisor
	Prof. dr. ir. R. Vos	TU Delft, Committee member

Cover: Military North American P-51 Mustang
Style: TU Delft Report Style, with modifications by Daan Zwaneveld

TU Delft

Preface

This thesis represents a significant milestone in my journey as an aerospace engineering student, a discipline that has always fascinated me with its blend of science, technology, and creativity.

I am deeply indebted to my supervisors, Woutijn Baars and Marios Kotsonis, whose guidance and expertise have been invaluable throughout this academic endeavour. Their wisdom has illuminated my path and inspired me to delve deeper into the intricacies of aerospace engineering. Their encouragement and constructive feedback have shaped this thesis into a comprehensive document that reflects the culmination of years of learning and exploration.

Furthermore, I would like to thank my family and friends for their unwavering support and encouragement. Their belief in my abilities has been a driving force, motivating me to overcome challenges and persevere in pursuing knowledge.

Sakariye Gudaal
Delft, March 2024

Summary

Traditional turbofan engines, reliant on aviation kerosene (Jet-A), remain integral for long-distance commercial flights due to their established reliability. Efforts within the aerospace sector are concentrated on optimising these engines, enhancing both efficiency and environmental sustainability. The emergence of electric aircraft signifies a transformative shift in aviation technology. Electric propulsion, predominantly powered by lithium-ion batteries, offers advantages such as reduced emissions, lower operational costs, and quieter flight operations. Presently, electric systems find application in short-range aircraft, primarily for regional and commuter flights. However, the limited energy density of current batteries necessitates ongoing advancements to extend the range and viability of electric aircraft for longer routes. Furthermore, hydrogen-based fuel cells present a promising alternative for mid-range missions. These fuel cells, generating energy through hydrogen, emit only water and heat as byproducts, ensuring ecological compatibility. Fuel-cell aircraft possess the capability to cover long distances, making them suitable for regional and transcontinental flights. However, challenges in thermal management emerge due to the inefficiencies in fuel cell stacks, necessitating innovative solutions to handle substantial heat loads effectively. One such solution is aerodynamic cooling with ducted, low-speed heat exchangers.

The thesis paper included a thorough investigation of the ducted radiator system, emphasising individual components and their performance characteristics. The investigation aimed to observe the effects the cooling duct subsystem has on the aircraft system as a whole. This is to discover whether this solution is viable in terms of managing the thermal payload while minimising the drawbacks of the subsystem, such as the increase in mass and drag. The product of this investigation is the construction of a numerical model of the cooling duct subsystem, which consists of a diffuser, a nozzle, and a heat exchanger. The investigation began with a detailed comparison of numerical findings and validation sources, which provided vital insights into the numerical model's correctness. While there was significant consistency, inconsistencies emerged owing to different assumptions, techniques, and particular model requirements. Notably, component fidelity discrepancies, particularly in the comprehensive evaluation of duct components, namely diffusers, nozzles, and heat exchangers, contributed to the observed disparities. These contrasts highlight the vital need for harmonising theoretical computations with experimental findings in future research endeavours for complete and accurate analysis of the cooling duct subsystem. Understanding the interconnected structure of duct components and the influence of changes in one area on the overall system are critical features of developing numerical models and advancing understanding of the researched system.

The paper then delves into the aircraft system performance, investigating alternative configurations such as decreased fuel, payload, and a balanced approach when the cooling duct subsystem is implemented. An in-depth examination revealed the limitations of single reductions: the lower fuel configuration severely reduced the aircraft's range by 48.6%, emphasising the importance of careful fuel management. The lowered payload option, on the other hand, demonstrated a very modest performance loss of 13.6% despite seating a lower number of people (24% capacity decrease), showing the trade-offs between cargo capacity and flying range. When both fuel and cargo weights were lowered concurrently, a fresh solution developed, transcending the restrictions associated with separate reductions. This balanced method increased the aircraft's range by 17.8% compared to the lower fuel configuration while retaining 88% of its conventional passenger capacity, providing a potentially viable answer for a wide range of flight missions and conditions. However, the paper noted that these conclusions were based on certain assumptions. It emphasised the significance of real-world testing to confirm these findings and fully unleash the potential of these combinations.

The numerical model indicates that not only are aerodynamic cooling ducts effective in heat dissipation, but they also offer advantages in terms of reduced pressure loss and drag, even thrust in some cases due to the Meredith effect. This efficiency is crucial for maintaining the powertrain's performance while minimising energy waste, making aerodynamic cooling ducts a sustainable and environmentally

friendly solution. This study not only affirms the viability of aerodynamic cooling ducts in the context of fuel cell-driven powertrains but also opens avenues for further research and development. The technical paper offered a thorough review of the complexities involved in optimising ducted radiator systems. It also provided useful insights for future research and engineering endeavours by merging theoretical computations with real observations, examining numerous configurations, and comprehending the multidimensional influence of many aspects.

Contents

List of Figures

List of Tables

Nomenclature

Abbreviations

Abbreviation	Definition
CFD	Computational Fluid Dynamics
FC	Fuel Cell
HAPSS	Hydrogen Aircraft Powertrain and Storage System
ISA	International Standard Atmosphere
LH2	Liquid Hydrogen
NACA	National Advisory Committee for Aeronautics
NTU	Number of Transfer Units
RANS	Reynolds Averaged Navier-Stokes
SFC	Specific Fuel Consumption
TMS	Thermal Management System
TOP	Take-off Parameter
WP	Work Package

Symbols

Symbol	Definition	Unit
$A_{c,i}$	Free-flow area	[m^2]
$A_{f,i}$	Fin area	[m^2]
$A_{fr,i}$	Frontal area	[m^2]
$A_{p,i}$	Primary area	[m^2]
$A_{t,i}$	Total area	[m^2]
A_w	Conduction area	[m^2]
b_i	Plate distance	[m]
b_r	Radiator thickness	[m]
c	Radiator tube length	[m]
c_d	Radiator drag coefficient	[-]
c_p	Power specific fuel consumption	[kg/kWhr]
$C_{c,tube}$	Jet contraction ratio	[-]
C_{D_i}	Drag coefficient	[-]
C_{L_i}	Lift coefficient	[-]
C_{max}	Max heat transfer capacity rate	[W/K]
C_{min}	Min heat transfer capacity rate	[W/K]
$C_{p,i}$	Specific heat @ const. pressure	[J/kg K]
C_{ratio}	Heat transfer capacity ratio	-
D_{cruise}	Cruise drag	[N]
$D_{h,i}$	Hydraulic diameter	[m]
D_i	Radiator drag	[N]
E_i	Radiator power	[W]
E_{HX}	Heat exchanger effectiveness	[-]
f	Friction coefficient	[-]
f_i	Friction factor	[-]
$f_{d,i}$	Circular tube friction factor	]-]
F_{net}	Net force	[N]

Symbol	Definition	Unit
g	Gravitational acceleration	[m/s^2]
G	Radiator mass velocity	[kg/m^{2}s]
G_i	Mass velocity	[kg/m^2 s]
h_i	Specific enthalpy	[J/kg]
$h_{i,c}$	Heat transfer coefficient	[W/m^2 K]
H_i	Flight altitude	[m]
H_{HX}	Heat exchanger height	m
j_i	Colburn factor	[-]
K_c	Contraction coefficient	[-]
$K_{d,tube}$	Velocity distribution coefficient	[-]
$K_{d,square}$	Square tube velocity distribution coefficient	[-]
K_e	Expansion coefficient	[-]
k_i	Thermal conductivity	[W/m K]
L	Radiator depth	[m]
L_{cruise}	Cruise lift	[N]
L_{HX}	Heat exchanger length	[m]
m	Mass	[kg]
m_i	m value	[-]
$\dot{m}$	Mass flow	[kg/s]
M	Mach number	[-]
n	Number of tubes	[-]
n_{f_i}	Number of fins	[-]
n_{off_i}	Number of offset strip fins	[-]
N	Number of transfer units	[-]
N_p	Number of passages	[-]
p_{f_i}	Fin pitch	[m]
p*	Normalised pressure	[Pa]
P_i	Pressure	[Pa]
Pr_i	Prandtl number	[-]
q_i	Dynamic pressure	[Pa]
q	Heat transfer	[W]
Q	Heat transfer	[W]
$\dot{Q}$	Volume flow	[m^3/s]
R	Gas constant	[J/mol K]
R_w	Thermal resistance	[W/K]
Re_i	Reynolds number	[-]
S	Intake area	[m^2]
t	Radiator tube pitch	[m]
t_{fin}	Fin thickness	[m]
t_{plate}	Plate thickness	[m]
T	Thrust	[N]
T_i	Temperature	[K]
U	Overall heat transfer coefficient	[W/m^2 K]
V_i	Velocity	[m/s]
W_{HX}	Heat exchanger width	[m]
α	Lapse rate	[K/m]
β	Nozzle exit opening ratio	[-]
δ	Normalised heat transfer	[-]
Δp_h	Mean dynamic pressure rise	[Pa]
η_f	Fin efficiency	[-]
η_i	Efficiency	[-]
η_o	Overall surface efficiency	[-]
γ	Specific heat ratio	[-]
ϕ_0	Discharge ratio	[-]

Symbol	Definition	Unit
ϕ_i	Airflow ratio	[-]
ρ_i	Density	[kg/m^3]
ρ_{fin}	Fin density	[1/m]
λ_i	Offset strip fin length	[m]
κ_i	Specific heat ratio	-
σ_i	Porosity	-

1 Introduction

Traditional combustion engines, particularly turbofan engines, continue to be the most popular choice for long-distance commercial flights. To generate thrust, these engines use aviation kerosene (Jet-A). Despite advances in electric and hydrogen propulsion, combustion engines presently provide the range and dependability required for transcontinental flights. The aircraft sector, on the other hand, is investing in research to make these engines more fuel-efficient and environmentally friendly.

Due to environmental concerns, many companies and government agencies in the aviation industry have shifted their focus to long-term solutions, namely electric aircraft. Electric aircraft marks a paradigm change in aviation, moving away from traditional internal combustion engines and towards electric propulsion technologies. These systems often use batteries as their major energy source, which has various benefits such as lower carbon emissions, lower operating costs, and quieter flight operations. Battery-powered propulsion systems are typically employed in short-range electric aircraft. These planes are frequently used for regional and commuter flights. Electric propulsion is powered by high-capacity batteries, most often lithium-ion batteries, which power electric motors that drive propellers or fans. During operation, these devices emit no emissions, making them environmentally friendly and excellent for decreasing the carbon footprint of short-haul flights. On the other hand, the poor energy density of modern batteries limits their applicability to small distances, often within a few hundred miles. Battery advancements are critical for improving range and making electric aircraft more feasible for longer routes.

Another solution is the use of liquid hydrogen (LH2) as a fuel source in fuel cell-powered powertrains for mid-range missions. These systems create energy using hydrogen fuel cells, which then drive electric motors for propulsion. The fundamental benefit of fuel cells over batteries is their high energy density and ability to refuel quickly. As byproducts, hydrogen fuel cells only emit water and heat, making them a clean and ecologically friendly solution. Fuel-cell aircraft can travel long distances, making them suited for regional and transcontinental trips. Efforts are being made to increase the efficiency, safety, and infrastructure for hydrogen generation and delivery. They do, however, bring a new set of issues, one of which is the thermal management system (TMS). When stacked, fuel cells currently have a maximum efficiency of 50-60%, implying that 40-50% of the energy produced is wasted. The majority of this waste is heat, which is an excessive amount to transfer into the surrounding air. Transferring this massive amount of heat to the ambient surroundings (i.e., thermal management) is a significant challenge to overcome, as traditional solutions are no longer applicable due to the different requirements that electric aircraft have in comparison to conventional aircraft.

One such factor is the location of heat generation. Electric motors and power electronics generate a substantial amount of heat in electric aircraft, which is distributed differently than in traditional aircraft. The concentrated heat sources in electric motors and power electronics require targeted and localised cooling solutions. In addition, traditional aircraft burn their fuel externally and incorporate natural cooling through airflow around the engine nacelles, whereas electric aircraft use batteries or fuel cells, which are internal components that generate substantial heat during operation and therefore require effective cooling strategies to manage temperature levels. Other factors to consider are the effects on the aircraft due to the changes in the airframe design when changing a conventional aircraft to an electric aircraft. These changes would affect the weight, stability, and performance of the aircraft. This, in turn, would affect the thermal payload generated and the required solution to optimise the efficiency and range of the aircraft.

To solve the thermal balance of future aircraft, ongoing research is being performed into enhanced cooling systems to increase thermal management efficiency, as well as innovative materials with higher thermal conductivity capabilities that can improve heat dissipation while lowering weight. One such solution to this problem is aerodynamic cooling with ducted, low-speed heat exchangers. Examples of aircraft with these cooling ducts are the Hy4 from H2FLY and the HAPSS system (Hydrogen Aircraft Powertrain and Storage Systems) from Conscious Aerospace.

(a) Hy4 from H2FLY[1]

(b) HAPSS system from Conscious Aerospace[2]

Figure 1.1: Examples of aircraft with cooling ducts obtained from the main websites of H2FLY and Conscious Aerospace

However, considering the cooling capacity required and the aerodynamic drag penalty, it is unclear whether this solution is viable. As a result, a detailed design of the duct system is required, as well as optimisation of the design in terms of aerodynamics, structures, thermodynamics, and performance. In addition, testing will be performed on the optimised duct design to evaluate the internal and exterior attributes of a given aircraft throughout its flight profile. This will establish if the duct's inclusion has a net positive or negative impact on the aircraft in question.

The main research question of this thesis is:

- *"How can the design of aerodynamic cooling ducts optimise thermal management in electric aircraft, with a particular focus on improving the cooling efficiency of fuel cell propulsion systems while considering factors such as weight, aerodynamics, and overall system performance?"*

A fuel-cell-powered airplane use case is necessary to determine the viability of this approach. For the sake of this project, the De Havilland Canada Dash 8-300, with a fuel-cell engine, will serve as the use case. The new powertrain is presently being built by Unified International's new company, Conscious Aerospace. The ability of the aerodynamic cooling ducts to completely transmit the heat produced by the Dash 8-300 will be put to the test, as well as how the increased drag will influence the aerodynamic performance of the aircraft. To answer this question, a set of sub-research questions is proposed, which are:

- *"How does the sizing of the diffuser inlet and nozzle outlet affect the aerodynamic drag penalty?"*
- *"What is the optimal sizing for the heat exchanger in the critical flight phase to maximise the amount of heat transferred from the fuel cell powertrain?"*
- *"How does the sizing of the diffuser inlet and nozzle outlet affect the heat transfer from the heat exchanger to the surrounding air?"*

[1] https://www.h2fly.de/

[2] https://www.consciousaerospace.com/

The main research objective of this thesis is:

- *“To investigate, analyse, and optimise the design of aerodynamic cooling ducts in electric aircraft, with the primary goal of improving the thermal management efficiency of fuel cell propulsion systems. This is done by constructing an analysis tool for the sizing and optimisation of the aerodynamic cooling duct while considering critical factors including weight constraints, aerodynamic impact, and overall system performance.”*

The diffuser, heat exchanger, and nozzle models will make up the analytical tool. To determine if the design is helpful or not, this model will examine the aerodynamic and thermal characteristics of these components. The following sub-objectives are established to fulfill this goal:

- *“To find out what the relationship between the duct design and the heat transfer from the heat exchanger is by comparing various design options in terms of efficiency through numerical analysis and/or model testing.”*
- *“To validate the analysis tool by comparing to existing research or experiments or by creating a demonstrator model of the cooling duct, carrying out a wind-tunnel test, and comparing the two sets of measurements.”*
- *”To find out the effect the cooling ducts have on the flight performance by evaluating the performance characteristics of an aircraft”*

The aircraft that will be investigated for the scope of this project is the De Havilland Canada Dash 8-300. The Dash 8-300 is a regional turboprop aircraft. It is currently being retrofitted with a fuel cell powertrain by Unified International’s new company, Conscious Aerospace. The aim of Unified is to collaborate with other innovative companies and institutions in the Netherlands to create the first hydrogen-powered operational aviation hub. What makes this aim unique is the adoption of Liquid Hydrogen as the main fuel source, which has a higher energy density and lower volumetric density compared to gaseous Hydrogen.

The structure of the literature report is organised as follows: Chapter 2 summarises previous literature on the current research topic and discusses how the goal of this thesis contributes to it. The methodology of the cooling duct subsystem and aircraft system that will be used in this project to achieve the research objectives and the test setup derived from the methodology are presented in chapter 3. In chapter 4, the verification and validation processes of the cooling duct subsystem are discussed. Chapters 5 and 6 discusses the results of the tests described in chapter 3. Finally, chapter 7 provides a summary of the findings from this report’s various chapters.

2

Literature Review

In this chapter, the literature on ducted radiators is presented and discussed.

2.1. Historical Background

In the 1930s, aircraft designers grappled with the escalating power of engines. This power spike posed a major challenge: effective waste heat removal, which resulted in drag and speed reduction. The drag caused by cooling systems was related to airspeed, potentially limiting the speed of piston-engine aircraft. Meredith's work [1] addressed this issue by suggesting two main strategies: first, delaying the cooling air before it reached the radiator/fins to decrease drag, and second, recovering waste heat energy to offset drag—a ground-breaking approach to minimising the cooling requirements of high-powered aviation engines.

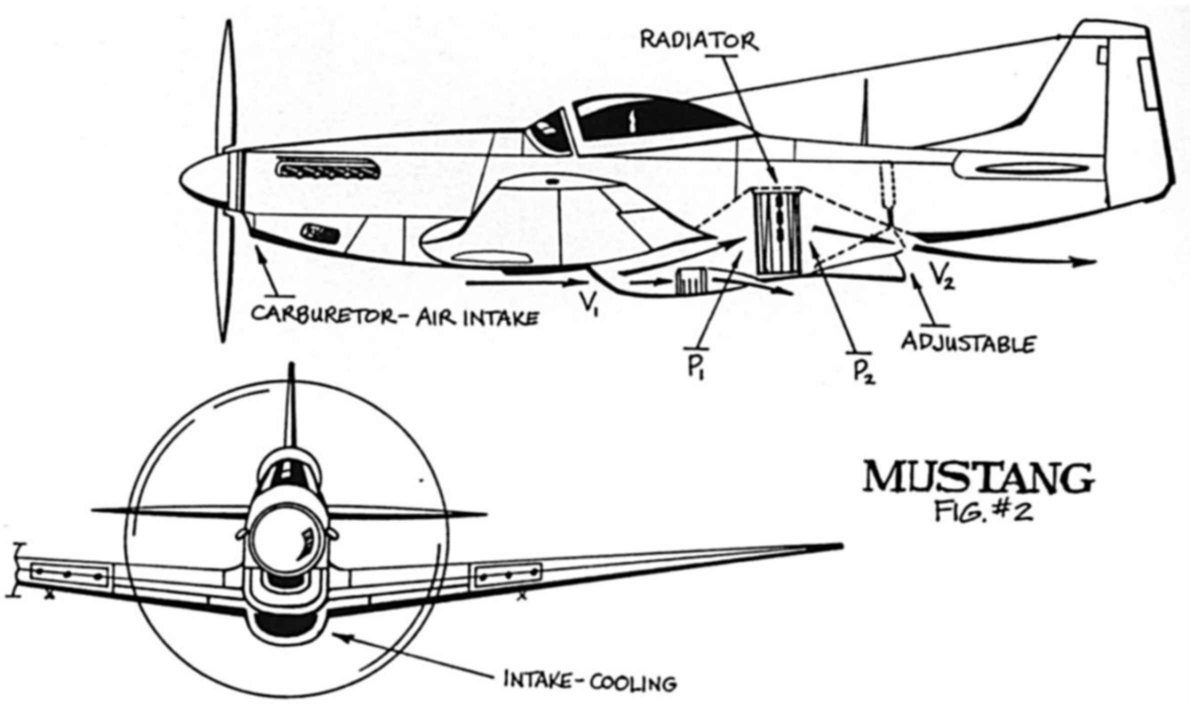

Figure 2.1: Schematic of the P-51 Mustang obtained from Atwood [2], highlighting the cooling duct

He came to the realisation that what was typically thought of as waste heat, to be transported to the environment by a coolant in a radiator, need not be wasted after thinking about the principles of liquid cooling [1]. With appropriate planning, the energy that the heat adds to the airflow may be utilised to produce thrust. After some testing, it was found that the reduction in thermal power and the drag penalty were lessened by Meredith's approach. This, combined with other scientific research supporting the idea conducted by H. Winter [3] and A. Silverstein [4], helped the idea acquire prominence during World War II.

The P-51 Mustang [2], the de Havilland Mosquito [5], and the Messerschmitt Bf 109 [6] are examples of how the concept is being used. However, the invention of jet engines rendered this concept obsolete. In recent years, the switch to more electrical aircraft has made this technology relevant once more, which has increased the thermal payload that needs to be eliminated.

Researchers using the Meredith effect in the design of piston engines in aircraft to improve efficiency and overall thrust are examples of this [7, 8]. Furthermore, F1 vehicles employ the Meredith duct, particularly at low speeds (less than 83 m/s). This is done to allow the heat exchanger to operate in both cross-flow and counter-flow modes [7].

2.2. Drag Determination

Meredith divided a cooling system's drag into three groups [1]. Which are:

1. The stream flow's skin friction drag
2. Stream separation-related drag caused by eddying
3. Drag caused by duct component expansion losses

This is done to separate the first drag component (i.e., the skin friction drag), as this component can be reduced [1] by reducing the wetted area or the velocity of the stream. By maximising the duct's streamlining, the other two drag factors may be disregarded. Notably, Meredith assumed that the fitted radiator has no exterior drag because it is housed inside a body or wing; hence, the drag components mentioned pertain to the internal stream of the cooling system.

Modelling the radiator as an actuator disc and assuming ideal gas conditions for the stream flow, it is determined that the stream through the radiator must reach the normal static pressure of the ambient freestream air [1]. As a result, it is impossible to lower the total pressure (static and dynamic) below the freestream static pressure.

2.2.1. Freely Exposed Radiator

Meredith distinguishes between two types of radiators: the freely exposed radiator and the ducted radiator. The radiator's drag (D_{23}), initially considering the freely exposed radiator, is described as follows:

$$D_{23,c} = A_2 \cdot (P_3 - P2) \tag{2.1}$$

where $(P_3 - P_2)$ is the radiator's pressure decrease and A_2 is the radiator's surface area. Efficiency is defined as the ratio of power used in the radiator ($E_{23,total}$) to power used to overcome drag (E_{23}):

$$\eta_{23,c} = \frac{E_{23}}{E_{23,total}} \tag{2.2}$$

Where the power components are:

$$E_{23,c} = \dot{Q}_2 \cdot (P_3 - P_2) = (P_3 - P_2) \cdot A_2 \cdot V_2 \tag{2.3}$$

$$E_{23,total,c} = (P_3 - P_2) \cdot A_2 \cdot V_0 \tag{2.4}$$

It is defined that $\dot{Q}_2$ is the volume flow of the stream, V_0 is the freestream velocity, and V_2 is the velocity through the radiator. After defining the power components, the efficiency is reduced to:

$$\eta_{23,c} = \frac{V_2}{V_0} \tag{2.5}$$

2.2.2. Ducted Radiator

The drag is different in the case of the ducted radiator, as extra forces are taken into account because of the duct's internal and exterior limits [1]. This is discovered by connecting the drag to the change in momentum rate:

$$D_{23,h} = A_2 \cdot \rho_0 \cdot V_0 \cdot V_2 \cdot \left(1 - \frac{V_4}{V_0}\right) = 2 \cdot \left(\frac{1}{2}\rho V^2\right) \cdot A_2 \cdot \left(1 - \frac{V_4}{V_0}\right) \cdot V_2 \tag{2.6}$$

Having identified the drag, the energy required to overcome it is:

$$E_{23,total,h} = 2 \cdot \left(\frac{1}{2}\rho V^2\right) \cdot A_2 \cdot V_2 \cdot \left(1 - \frac{V_4}{V_0}\right) \tag{2.7}$$

The power utilised by the radiator is the same as equation 2.3, so the ducted radiator efficiency is determined as:

$$\eta_{23,h} = \frac{E_{23,h}}{E_{23,total,h}} = \frac{(P_3 - P_2)}{2 \cdot \left(\frac{1}{2}\rho V^2\right) \cdot \left(1 - \frac{V_4}{V_0}\right)} \tag{2.8}$$

2.2.3. Concluding Remarks

It was discovered that the optimal efficiency of ducted radiators is 50% more than that of (at the time) conventional radiators and that the power necessary to overcome drag is around 2/3 of the power required with the freely exposed radiator. Depending on the size of the radiator, it has also been shown that combining the effects of compressibility and heat transfer from the radiator can reduce power usage to zero [1]. Using the heat from the exhaust might also potentially reduce the drag created and increase thrust. However, the paper only focuses on the effects of the radiator. The effects of the duct components (i.e., the diffuser and nozzle) were not considered. These effects would contribute to the overall effect on the total internal net force generated. In addition, the paper is purely based on theoretical computation. Although this is understandable as this technical report is the first to investigate this concept, it did not provide experimental data to support or expand the theory on ducted radiators.

2.3. Past Research On Ducted Radiators

Winter developed a method to calculate the reduction in mass flow and drag of a heated radiator under actual operating conditions versus its cold state. This approach takes into account many parameters and applies to both symmetrical and unsymmetrical radiator configurations used in aircraft structures. The goal of this work is to create simple formulas for a more accurate estimation of the decrease in radiator drag due to heating based on Meredith's insights into the possible power gain under operating circumstances. The emphasis is on utilising velocity-pressure diagrams to depict the influence of air forces on a duct radiator, particularly the radiator cowling. The purpose is to give realistic and reliable estimates of changes in radiator performance under various operating conditions, considering both cold and hot radiator states. Figure 2.2 shows an illustration of a ducted radiator.

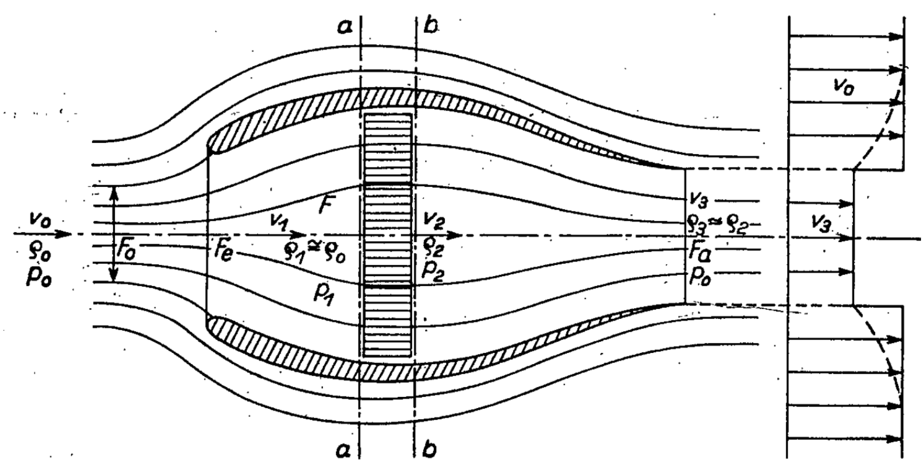

Figure 2.2: Flow through and around a ducted radiator, obtained from Winter [3]

The paper also focuses on estimating the decrease in the discharge rate and internal drag for radiators with varying drag coefficients and thermodynamic efficiencies under different heating conditions. The method involves the estimation of these parameters as a function of the duct opening ratio. The decrease in internal drag indicated a reduction in the resistance to airflow within the radiator [3], which can have positive implications for the overall efficiency and performance of the aircraft system. Additionally, the decrease in discharge rate suggested a change in the mass flow of air through the radiator, which can influence the thermal and aerodynamic characteristics of the system.

In comparison to Meredith's [1] paper, the evaluation of the internal drag is more extensive as it takes into account the effects of momentum and energy conservation for not only the radiator but also the duct components. When varying the duct opening ratios, it was observed that decreasing the ratio reduces the internal drag significantly, until it eventually becomes non-existent [3]. However, if steps are not taken to decrease the external drag by optimising the mounting procedure within the fuselage or wing, this design might result in a significant external drag [3]. Although these improvements are beneficial to understanding this concept better, it is still only theoretical. To improve the concept and apply it to existing aircraft, it is necessary to conduct experiments. A. Silverstein carried out such tests [4].

The tests conducted by A. Silverstein are another contribution to the Meredith duct. To study the partial recovery of waste thermal energy during the cooling of aircraft engines, he performed wind tunnel tests on models of ducted radiators. Figure 2.3 shows a depiction of the test model.

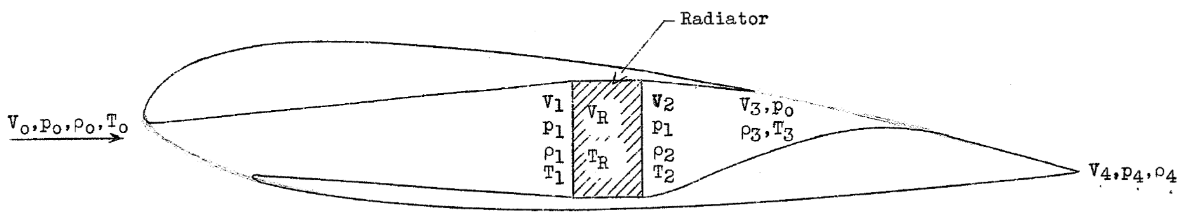

Figure 2.3: Schematic of the wind-tunnel test model, obtained from Silverstein [4]

The drag, quantity of airflow via the duct, air temperature rise across the heater, static pressure at the heater, and electrical input were all measured during the experiments [4]. The ducts were examined, and the electrical heater utilised in the duct was made out of grids of flat bars coupled together to absorb the available power. The temperatures of the air behind the heater were monitored using four calibrated thermocouples [4], as was the amount of air moving through the duct. A vertical rack of thermocouples was also used to monitor the temperature of the air in the wake behind the wing to calculate the distribution of heat over the wake.

When comparing the two, the measured values of drag and heat content had a strong connection with the assumptions established [4]. The figure below depicts a summary of the test results for various duct configurations:

Table 2.1: Summary of test results from wind tunnel experiments [4]

Duct	C_d cold [-]	C_d hot [-]	ΔC_d [-]
1	0.0147	0.0127	0.0020
2	0.0154	0.0133	0.0021
3	0.0180	0.0159	0.0021
4	0.0187	0.0164	0.0023

This demonstrates that the drag decrease while adding heat is around 0.002 for all duct layouts. This difference, from around 10% to 15% of the section-drag coefficient of the wing and duct, was therefore measured with great precision [4]. This also proves that the concept that Meredith and Winter investigated can apply to existing aircraft, such as the P-51. However, with the current need to investigate how the concept can be applied to modern electric aircraft, it would be beneficial to integrate the developed formulas into a numerical aircraft design tool. This integration would streamline the practical application of the method in the aircraft design process, allowing engineers and designers to easily incorporate radiator drag calculations into their analyses. By becoming part of established design workflows, the method can contribute to more efficient and informed decision-making during the early stages of aircraft design, particularly for electric aircraft.

In addition to constructing a numerical tool, the data collected needs to be reliable. One can validate the accuracy and reliability of the derived formulas by conducting a thorough comparison with Computational Fluid Dynamics (CFD) simulations. Using this approach will allow for a detailed examination of the radiator's aerodynamic characteristics and heat transfer dynamics under various operating conditions. This comparative analysis serves as a critical step to assess the validity of the simplified formulas and to identify potential discrepancies or areas where further refinement may be necessary. A robust comparison with CFD results will enhance confidence in the method's predictive capabilities and broaden its applicability in the field of aerospace engineering. The first step to applying this approach is to look at more recent literature that has investigated the Meredith effect in modern aircraft. This is done in section 2.4.

2.4. Modern Evaluation Of Ducted Radiators

Before the shift to more electrical aircraft, piston engines were a popular choice as the powertrain for aircraft due to their high efficiency and flexibility in using various fuels (e.g., Diesel, JP4, JP8, etc.). In 2007, L. Piancastelli and M. Pellegrini investigated the Meredith effect as a way to improve the performance of piston engines [7]. The use case for their case was a comprehensive study on the VD007 hybrid turbo-diesel engine, designed for the C-130J airplanes. The study aims to increase the total thrust of the engine while eliminating radiator drag. The diffuser design involved considerations of length, angle of divergence, and the positioning of the air intake near the propeller to optimise airflow and reduce losses. Additionally, the study references the work of Gothert, who highlighted the importance of minimising drag in the diffuser to optimise airflow into the duct. The design also included the use of inlet and outlet guide vanes to enhance efficiency.

The design of the radiator for the VD007 engine involved considerations of a basic formula for dimensioning the radiator, the type of radiator, and the impact of the radiator shape on the total thrust of the system. The study provided detailed information on the dimensions, weights, and air characteristics of the principal and oil radiators, which were crucial in the design process. The radiator shape was found to improve the total thrust and eliminate radiator drag, contributing to the overall performance of the engine's cooling system. The design of the nozzle for the VD007 engine involved considerations of its impact on the drag coefficient of the radiator, the heating effect on nozzle thrust, and the dimensions and characteristics of the nozzle. The study discussed the negligible impact of both distributed and concentrated losses on the nozzle and emphasised the importance of evaluating the influence of the nozzle on the drag coefficient of the radiator. The properties of the duct can be seen in table 2.2:

Table 2.2: VD007 duct data, obtained from Piancastelli et al. [7]

Section	Pressure [Pa]	Velocity [m/s]	Temperature [K]
1	32758.8	231.1	232.44
2	61570.0	25.1	263.0
3	56324.0	35.5	341.0
4	32758.5	309.3	292.08

The study highlights that, due to the Meredith effect, the cooling system not only eliminates radiator drag but also increases the total thrust of the system by about 2400 N at cruise speed. This finding underscores the potential of the cooling system to enhance the performance of aircraft piston engines, making them more attractive for aeronautical applications. Additionally, the study estimates a reduction in drag of about 650 N due to the increase in radiator drag being counteracted by the heating effect on the nozzle thrust.

Another study by L.Piancastelli et. al. [8] aimed at recuperating wasted heat in piston engine cooling. It explores various designs and approaches, providing a comparative analysis of their performance and efficiency. The study focuses on the Meredith duct, examining its pressure drop, temperature increment, and power ratio. This analysis sheds light on the potential benefits and drawbacks of the Meredith Ramjet in comparison to other cooling systems (i.e., Under-fuselage/under-nacelle vs. in-wing layouts). The document also discusses the additional thrust generated by the cooling system and its potential implications for the design and performance of piston engine propulsion systems. An overview of the duct properties can be seen in table 2.3:

Table 2.3: Ramjet duct data, obtained from Piancastelli et al. [8]

Section	Pressure [Pa]	Velocity [m/s]	Temperature [K]	Enthalpy [kJ/kg]
0	54019.9	152.9	255.65	267.3
1	61644.2	30.6	263.15	339.15
2	54185	44.8	338.15	339.15
3	54019.9	296	276.9	336

When the temperature rises, the configuration of the duct design may alter. A thicker radiator is necessary when increasing the radiator temperature [8]. Because of the increased pressure drop, a longer duct is required to recover more pressure in the diffuser. This lengthening affects the duct's weight and drag. As a result, a higher power output is necessary. It is noted that around 200 degrees, the power increment starts to plateau, so the focus should be on reducing the aerodynamic drag of the duct at this point. The added thrust of the cooling system boosts interest in piston engine propulsion in the aviation industry. In reality, thanks to the Meredith effect, it was feasible to reduce radiator drag and boost the total thrust [8] of the power pack. As a result, the Meredith ramjet boosts total available thrust while decreasing fuel consumption.

Under-fuselage/under-nacelle and in-wing layouts were both studied. The in-wing system with its low aspect ratio radiators appears to be the best alternative [8] for reducing duct external drag and improving lift at takeoff. The option of a lengthy high-temperature duct in the under-fuselage/under-nacelle does not provide substantial gains in efficiency and thrust. Furthermore, greater coolant temperatures and bigger radiators add significantly to the total weight [8] of the Meredith ramjet. Thicker radiators necessitate longer diffusers and more duct drag.

These papers that evaluated the Meredith effect on piston engines showed that ducted radiators could potentially be a viable option for electric aircraft due to the noted improvements in thermal management and drag decrease/thrust increase. However, they used a combination of theory and experimental data to obtain their results, which cannot be easily replicated. Hence, it is necessary to create a numerical tool to evaluate the duct as a whole. In addition, they provided data, such as tables 2.2 and 2.3, that could be used as validation of the numerical tool

3
Methodology

This chapter discusses the methodology used to create the numerical tool and presents the tests that will be carried out using said tool.

3.1. Concept On Ducted Radiators

The concept of ducted radiators is discussed in this section.

3.1.1. Function

The ducted radiator can be modelled as shown in figure 3.1:

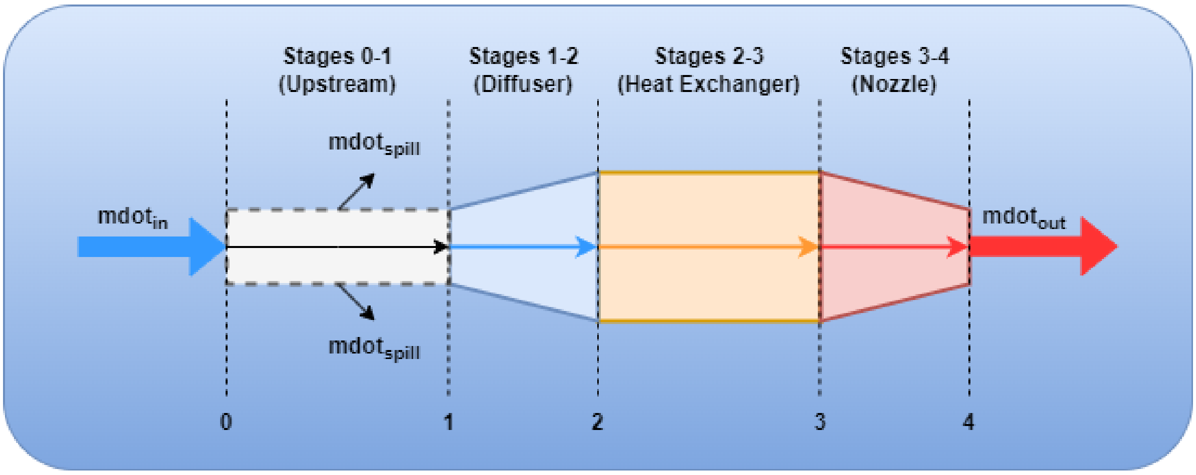

Figure 3.1: Model of the ducted radiator

The process begins with air (stage 0) entering through a well-designed inlet (stage 1), ideally one that allows fast-moving air to smoothly enter the diffuser without creating turbulence. However, if the air enters too quickly or if there are abrupt changes in geometry or flow conditions, it can spill over the edges of the diffuser, leading to inefficiencies and loss of performance (i.e., mass flow spill). Once inside, the air encounters an expanding chamber towards the diffuser outlet (stage 2). According to Bernoulli's principle, the air within the chamber experiences a speed reduction and, concurrently, an increase in pressure [8, 9]. This phenomenon occurs because the kinetic energy of the incoming air is transformed into potential energy through the compression of the air, leading to a rise in pressure within the diffuser.

The compressed and decelerated air then passes via a radiator (stages 2–3), where it cools a working fluid (a mixture of water and ethylene glycol). This cooled fluid is then sent to the engine, where it serves a crucial role in managing engine temperature while the engine is operating. The passage of air through the radiator, on the other hand, is not straightforward; the air experiences resistance as it navigates around tubes and fins within the heated radiator [8, 9]. The pressure created in the diffuser is what forces the air through the radiator. Unfortunately, part of the diffuser pressure is lost during this process. Therefore, it is necessary to design the radiator in such a way that only a minimal amount of pressure is lost, ensuring that the pressure on the rear face (stage 3) of the radiator remains relatively close to that on the front face (stage 2).

Finally, as the air enters the nozzle (stages 3–4), the pressure built up in previous phases, as well as the heat generated by the radiator, becomes critical. The nozzle undergoes thermodynamic expansion, where the energy from compression and heat is converted into kinetic energy when the air passes through the nozzle [8, 9]. Simply put, the nozzle promotes the conversion of stored potential energy into kinetic energy, driving the air through the nozzle at greater speeds. The increase in kinetic energy in an aircraft results in a change in air momentum, known as thrust. The duct system is dragged along due to its role and effort in working against air viscosity. Meredith demonstrated that the thrust extracted from the heated air could exceed the drag of the entire cooling system, provided the aircraft was flying at over 300 mph [1].

3.1.2. Assumptions

The following assumptions are made when modelling a simple ducted radiator:

- 2D Axis-symmetric model
- Quasi-1D flow
- Fluid is ideal and has uniform fluid properties
- The process in the diffuser and nozzle is adiabatic and isentropic.
- The freestream air flow area is equal to the diffuser inlet area (as shown in figure 3.1)
- Constant heat transfer coefficients
- No phase changes
- No mixing of fluids
- The interaction between the hot and cold fluids is cross-flow.
- Constant fluid flow rates and uniform flow distribution
- No air will leak out of the duct throughout the process.

3.1.3. Operating Conditions

When considering the operating conditions that are most critical when designing the aerodynamic cooling duct, the two most significant stages of the flight phase are the take-off/climb phase and the cruise phase.

The take-off and climb phases impose significant demands on the aircraft's engines, requiring high power settings and generating increased heat. They are also critical for engine performance, as efficient cooling is essential to ensuring that the engines operate within their temperature limits and deliver the required power for a safe and successful climb. In addition, climbing through different altitudes and potential temperature variations during climb-out introduces challenges for cooling as the system has to adapt to these variations and ensure consistent cooling performance. Lastly, safety considerations have to be made, especially for take-off, as engine reliability is of utmost importance.

During the cruise phase, aircraft operate at high altitudes and speeds, with engines operating at a sustained power level. The cooling system needs to operate reliably and continuously to maintain optimal engine performance. Fuel efficiency is crucial, and effective cooling with ducted heat exchangers helps maintain optimal engine performance. Efficient aerodynamics also help maintain the aircraft's fuel efficiency. By designing optimised ducted heat exchangers, it's possible to minimise drag and effectively dissipate heat, ensuring efficient aerodynamics and fuel efficiency.

Although both take-off and climb phases are crucial, the take-off/climb phase may be more critical due to higher power demands, safety considerations, and the dynamic nature of the phase changes. However, the overall design concept for the cooling system is to ensure robust performance across the entire flight envelope. This means that the cooling system must be capable of handling all the challenges posed by different flight phases to ensure the safety, reliability, and efficiency of the aircraft.

3.1.4. Numerical Model Construct

The numerical model is constructed using four main functions. The functions are:

- The upstream
- The diffuser
- The heat exchanger
- The nozzle

The purpose of the upstream function is to determine the ambient conditions of the air that will enter the diffuser inlet. This is done by combining the ISA (International Standard Atmosphere) method and isentropic expansion. The diffuser function uses the upstream function outputs as inputs to determine the air properties of the diffuser outlet using isentropic relations. In addition, the function determines the mass of the diffuser using its dimensions and material properties.

The heat exchanger function determines its size and performance in exhausting heat away from the aircraft's propulsion system. Using a compact heat exchanger design approach, particularly one for a plate-finned heat exchanger, and the effectiveness-NTU method, an accurate depiction of the heat exchanger can be achieved. The nozzle function follows a similar approach to the diffuser function in that the air properties and mass are computed using isentropic relations and geometrical calculations. However, the nozzle function also determines the total internal net force using a variation of the thrust equation.

As each subsequent function requires the input of the preceding function and the nozzle function outputs are required for the upstream function (as described in section 3.2), the functions are coupled in an iterative process, as shown in figure 3.2:

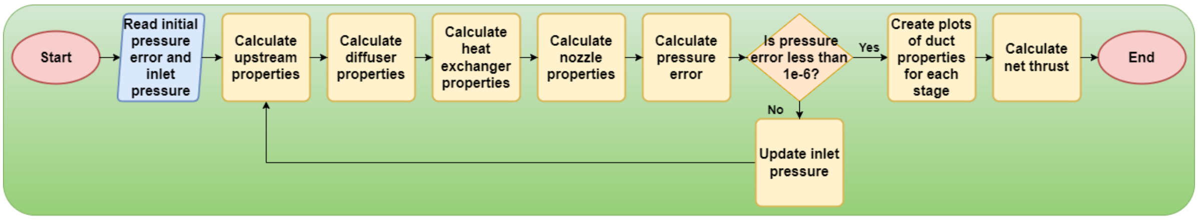

Figure 3.2: Flow chart of the numerical model of the cooling duct subsystem

The figure above is a general representation of the numerical model. In section 3.2, the functions are described in detail, and the use of the numerical tool is described in section 3.3.

3.2. Internal Analysis Of The Cooling Duct

In this section, the fundamental knowledge of the internal effects of the duct is outlined.

3.2.1. Ambient Air (Stages 0-1)

The first step is to use the altitude to determine the static ambient air conditions. This can be calculated using the ISA (International Standard Atmosphere) method [10]. First, the static temperature and pressure are found with equations 3.1 and 3.2:

$$T_0 = T_{SL} + \alpha \cdot (H_0 - H_{SL}) \tag{3.1}$$

$$P_0 = P_{SL} \cdot \left(\frac{T_0}{T_{SL}}\right)^{\left(\frac{-g}{\alpha \cdot R}\right)} \tag{3.2}$$

Where T_{SL}, P_{SL}, and H_{SL} are the sea level ambient temperature (288.15 K), ambient pressure (101325 Pa), and altitude (0 m). In addition, g, R, and α are the gravitational acceleration (9.81 m/s^2), the gas constant (287 J/kg K), and the lapse rate.

With the ambient properties calculated, the duct inlet properties can be determined. Assuming that the duct is a closed system, the ambient pressure and exit pressure are equal ($P_4 = P_0$). Therefore, an iterative process is required to ensure this constraint. This is done by updating the inlet pressure (P_1) with the following equation:

$$P_1 = P_1 + 0.1 \cdot (P_0 - P_4) \tag{3.3}$$

With a value of P_1 defined, the inlet temperature and velocity can be determined:

$$T_1 = T_0 \cdot \left(\frac{P_1}{P_0}\right)^{\frac{\kappa_a - 1}{\kappa_a}} \tag{3.4}$$

$$V_1 = \sqrt{\left(2 \cdot \left[\frac{V_0^2}{2} + h_0 - h_1\right]\right)} \tag{3.5}$$

$$\tag{3.6}$$

Where h_0 and h_1 are the specific enthalpies at the ambient air and inlet of the duct. The mass flow is determined to be:

$$\rho_1 = \frac{P_1}{R \cdot T_1} \tag{3.7}$$

$$\dot{m}_0 = \rho_0 \cdot A_0 \cdot V_0 \quad , \quad \dot{m}_1 = \rho_1 \cdot A_1 \cdot V_1 \quad \rightarrow \quad \dot{m}_{spill} = \dot{m}_0 - \dot{m}_1 \tag{3.8}$$

Where A_0 is assumed to be the same as A_1.

3.2.2. Diffuser (Stages 1-2)

Knowing the properties at the inlet of the diffuser (stage 1) and assuming the inlet mass flow is constant ($\dot{m}_2$ = $\dot{m}_1$) as no air escapes, the law of conservation [11] can be used to determine the velocity at the outlet of the diffuser:

$$\dot{m}_1 \left(h_1 + \frac{V_1^2}{2}\right) = \dot{m}_2 \left(h_2 + \frac{V_2^2}{2}\right) \tag{3.9}$$

$$\dot{m}_2 = \dot{m}_1 \quad \rightarrow \quad h_1 + \frac{V_1^2}{2} = h_2 + \frac{V_2^2}{2} \tag{3.10}$$

Where h_2 is the specific enthalpy at the outlet of the diffuser. Assuming the flow decelerates to the point where the kinetic energy is negligible ($V_1 = 0$), and that no air escaped (so the mass flow stays constant), the energy conservation equation becomes:

$$h_2 = h_1 + \frac{V_1^2}{2} \tag{3.11}$$

Where C_p is the specific heat capacity at constant pressure. With this term and using isentropic relations [11], the properties of the diffuser outlet can be calculated:

$$T_2 = \frac{h_2}{C_p} V_2 = V_1 \cdot \left(\frac{T_2}{T_1}\right)^{\frac{1}{1-\kappa_a}} \tag{3.12}$$

$$P_2 = P_1 \cdot \left(\frac{T_2}{T_1}\right)^{\frac{\kappa_a}{\kappa_a - 1}} \tag{3.13}$$

$$\rho_2 = \frac{P_2}{R \cdot T_2} \tag{3.14}$$

Finally, to determine the mass of the diffuser (m_{diff}), the following equation is used:

$$\begin{aligned} V_{diff} &= ((0.5 \cdot (H_{HX} + H_{diff}) \cdot L_{diff}) \cdot W_{HX} \\ &\quad - (0.5 \cdot (H_{HX} + H_{diff} - 4 \cdot t_{diff}) \cdot (1 - 2 \cdot t_{diff}) \cdot (W_{HX} - 2 \cdot t_{diff}))) \end{aligned} \tag{3.15}$$

$$m_{diff} = \rho_{Al} \cdot V_{diff} \tag{3.16}$$

Where H_{HX} and W_{HX} are the height and width of the heat exchanger, H_{diff}, L_{diff}, and t_{diff} are the height, length, and thickness of the diffuser inlet, and ρ_{Al} is the density of Aluminium.

3.2.3. Heat Exchanger (Stages 2-3)

The heat exchanger's purpose is to cool down the hot coolant coming from the aircraft to the ambient air's operating temperature. The method used to determine the sizing of the heat exchanger is the compact heat exchanger approach. In particular, the plate-finned heat exchanger is used as the model.

Plate-fin heat exchangers are used to improve heat transfer between fluids, particularly between air and gas. They use various geometries such as triangular, rectangular, wavy, offset strip, louvred, and perforated fins. Among these, the offset strip fin type is the most common. Plate-fin heat exchangers have been used since the 1910s in the automotive sector and the 1940s in the aerospace industry [12, 13]. They are now used in a variety of sectors, including airplanes, cryogenics, gas turbines, nuclear, and fuel cells.

These heat exchangers are intended for working pressures less than 700 kPa and have surface area densities of up to 5900 m2/m3. The fin thickness normally ranges between 0.05 and 0.25 mm, with fin heights ranging between 2 and 25 mm. Fin density is typically between 120 to 700 fins per metre, while specific applications require as many as 2100 fins per metre [12]. The schematic of the plate-fin heat exchanger can be seen in figure 3.3:

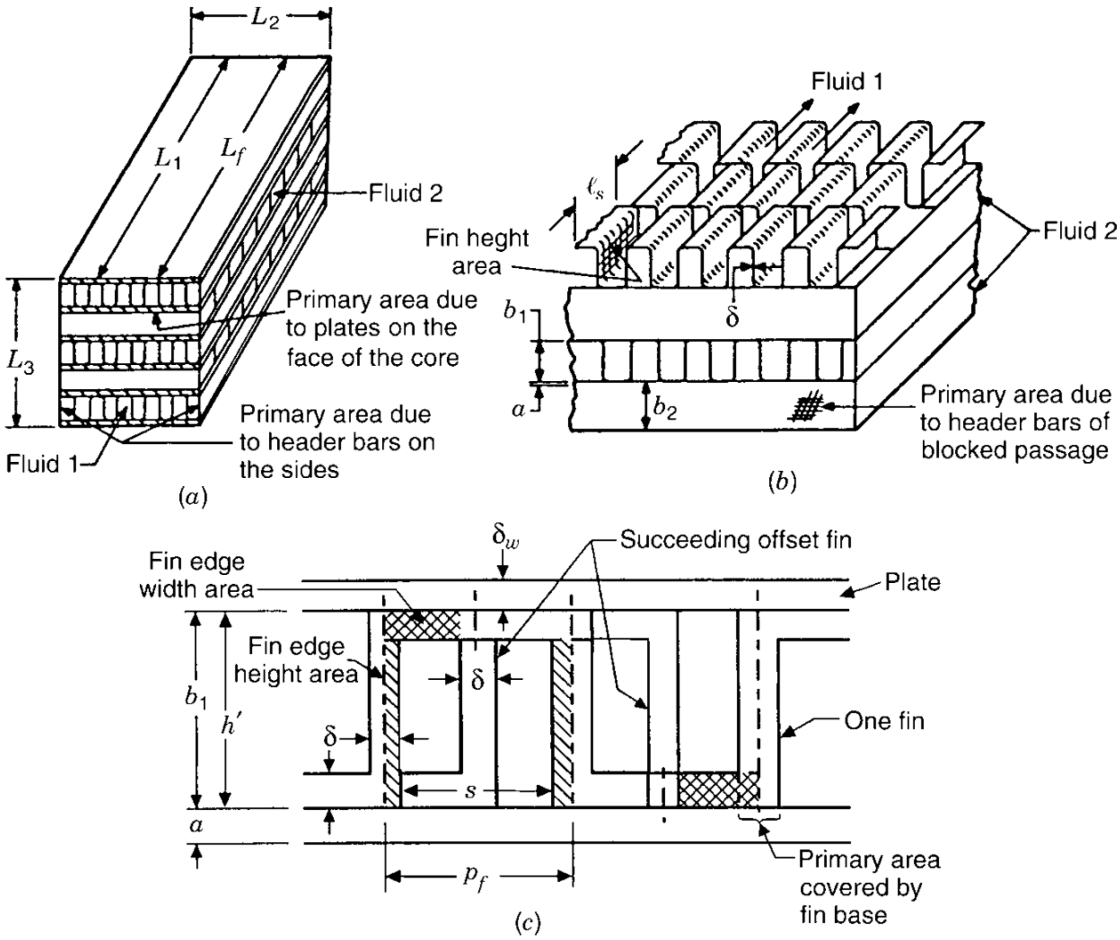

Figure 3.3: (a) Plate-fin exchanger; (b) offset strip fin geometry; (c) small section of an idealized offset strip fin geometry [12]

Geometry

In the analysis, the total heat transfer area for each fluid is critical. It is divided into two sections: the primary area (A_p) and the fin area (A_f). The plate area, excluding the fin base region, as well as the multi-passage side walls and multi-passage front and back walls, comprise the major area [12, 13]. A simplified schematic of part of the plate-fin heat exchanger can be seen in figure 3.4:

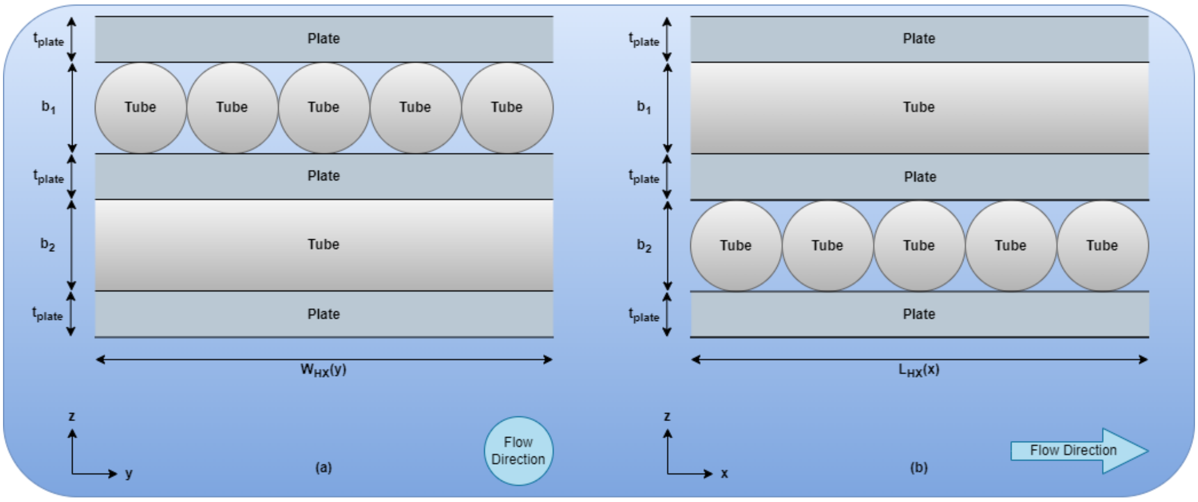

Figure 3.4: Simplified schematic of the front (a) and side (b) view of the plate-fin heat exchanger

The total number of passages can be obtained with equation 3.17:

$$N_p = \frac{H_{HX} - b_2 - 2 \cdot t_{plate}}{b_1 + b_2 + 2 \cdot t_{plate}} \tag{3.17}$$

Where b_1 and b_2 are the plate distance for each fluid, and t_{plate} is the thickness of the plate. The total number of fins for both fluids is:

$$n_{f_1} = \frac{W_{HX}}{t_{fin} + b_1} \quad , \quad n_{f_2} = \frac{L_{HX}}{t_{fin} + b_2} \tag{3.18}$$

Where W_{HX} and H_{HX} are the width and height of the heat exchanger, and t_{fin} is the fin thickness. Using these values, the fin pitch can be determined:

$$\rho_{fin,1} = n_{f_1} \cdot \frac{t_{fin}}{W_{HX}} \quad \rightarrow \quad p_{f_1} = \frac{1}{\rho_{fin,1}} \tag{3.19}$$

$$\rho_{fin,2} = n_{f_1} \cdot \frac{t_{fin}}{W_{HX}} \quad \rightarrow \quad p_{f_2} = \frac{1}{\rho_{fin,2}} \tag{3.20}$$

As stated before, the total main area is calculated by removing the fin base areas from the total plate areas and then adding the passage side wall areas, front and rear wall areas, and passage front and back wall areas. This is shown in equations 3.21 and 3.22:

$$\begin{aligned} A_{p_1} &= (2 \cdot W_{HX} \cdot L_{HX} \cdot N_p) - (2 \cdot t_{fin} \cdot L_{HX} \cdot n_{f_1}) \\ &\quad + (2 \cdot b_1 \cdot L_{HX} \cdot N_p) + (2 \cdot [b_2 + 2 \cdot t_{plate}] \cdot W_{HX} \cdot [N_p + 1]) \end{aligned} \tag{3.21}$$

$$\begin{aligned} A_{p_2} &= (2 \cdot W_{HX} \cdot L_{HX} \cdot [N_p + 1]) - (2 \cdot t_{fin} \cdot L_{HX} \cdot n_{f_2}) \\ &\quad + (2 \cdot b_2 \cdot W_{HX} \cdot [N_p + 1]) + (2 \cdot [b_1 + 2 \cdot t_{plate}] \cdot L_{HX} \cdot N_p) \end{aligned} \tag{3.22}$$

The number of offset strip fins is defined by:

$$n_{off_1} = \frac{L_{HX}}{\lambda_1} \tag{3.23}$$

$$n_{off_2} = \frac{W_{HX}}{\lambda_2} \tag{3.24}$$

Where λ_1 and λ_2 are the offset strip fin lengths for fluids 1 and 2. Using these terms, the total fin areas are:

$$\begin{aligned} A_{f_1} &= (2 \cdot [b_1 - t_{fin}] \cdot L_{HX} \cdot n_{f_1}) \\ &+ ([p_{f_1} - t_{fin}] \cdot t_{fin} \cdot [n_{off_1} - 1] \cdot n_{f_1}) \\ &+ (2 \cdot p_{f_1} \cdot t_{fin} \cdot n_{f_1}) \end{aligned} \tag{3.25}$$

$$\begin{aligned} A_{f_2} &= (2 \cdot [b_2 - t_{fin}] \cdot W_{HX} \cdot n_{f_2}) \\ &+ ([p_{f_2} - t_{fin}] \cdot t_{fin} \cdot [n_{off_2} - 1] \cdot n_{f_2}) \\ &+ (2 \cdot p_{f_2} \cdot t_{fin} \cdot n_{f_2}) \end{aligned} \tag{3.26}$$

In this case, fluid 2 is a 50:50 mixture of water and ethylene glycol, so the fluid passes through tubes. However, this tube will pass through a series of fins ($A_{f,2}$) to enhance the contact area with the outside fluid (i.e. air). The dimensions of the tube are determined by the spacing provided by the dimensions of the heat exchanger and fins, namely the defined volume for each fluid, which is defined by:

$$V_{p_1} = b_1 \cdot W_{HX} \cdot L_{HX} \cdot N_p \tag{3.27}$$

$$V_{p_2} = b_2 \cdot W_{HX} \cdot L_{HX} \cdot (N_p + 1) \tag{3.28}$$

With V_{p_2} calculated, the diameter of the glycol tube is:

$$D_{gl,tube} = \sqrt{\frac{4 \cdot V_{p_2}}{(N_p + 1) \cdot \pi \cdot W_{HX}}} \tag{3.29}$$

With the primary areas and fin areas determined, the total surface area can now be calculated:

$$A_{t_i} = A_{f_i} + A_{p_i} \tag{3.30}$$

The free-flow area can be calculated by subtracting the area obstructed by the fins at the core's entry on that side from the frontal area

$$A_{c_1} = (b_1 - t_{fin}) \cdot (p_{f_1} - t_{fin}) \cdot n_{f_1} \tag{3.31}$$

$$A_{c_2} = (b_2 - t_{fin}) \cdot (p_{f_2} - t_{fin}) \cdot n_{f_2} \tag{3.32}$$

Where the frontal area is determined using the following equations:

$$A_{fr_1} = W_{HX} \cdot H_{HX} \tag{3.33}$$

$$A_{fr_2} = L_{HX} \cdot H_{HX} \tag{3.34}$$

Finally, the mass of the heat exchanger can be determined [14]:

$$\begin{aligned} V_{HX} &= [n_{rows} + (n_{rows} + 1) + 1] \cdot L_{HX} \cdot W_{HX} \cdot t_{plate} \\ &+ n_{rows} \cdot (b_2 + p_{f_2} - t_{fin}) \cdot L_{HX} \cdot t_{fin} \cdot (W_{HX}/p_{f_2}) \\ &+ (n_{rows} + 1) \cdot (b_1 + p_{f_1} - t_{fin}) \cdot W_{HX} \cdot t_{fin} \cdot (L_{HX}/p_{f_1}) \end{aligned} \tag{3.35}$$

$$m_{HX} = \rho_{Al} \cdot V_{HX} \tag{3.36}$$

Where n_{rows} are the number of layers of the heat exchangers.

Heat Transfer

With the geometry of the heat exchanger defined, it is necessary to carry out the determination of the heat transfer performance. This is first done by defining the heat transfer coefficient.

Convective Heat Transfer Coefficient

In terms of friction considerations, this design provides good heat transmission performance. There have been several research using analytical, numerical, and experimental investigations throughout the last 50 years. Manglik and Bergles [15] reported the most extensive correlations for the j (Colburn) and f (friction) variables in the laminar, transition, and turbulent regions in 1995. The Reynolds number at which transition occurs is at 2300.

For the laminar region, the Colburn and friction factors are:

$$j_i = 0.6522 \cdot Re_i^{-0.5403} \cdot \left(\frac{p_{f_i} - t_{fin}}{b_i - t_{fin}}\right)^{-0.1541} \cdot \left(\frac{t_{fin}}{\lambda_i}\right)^{0.1499} \cdot \left(\frac{t_{fin}}{p_{f_i} - t_{fin}}\right)^{-0.0678} \tag{3.37}$$

$$f_i = 9.6243 \cdot Re_i^{-0.7422} \cdot \left(\frac{p_{f_i} - t_{fin}}{b_i - t_{fin}}\right)^{-0.1856} \cdot \left(\frac{t_{fin}}{\lambda_i}\right)^{0.3053} \cdot \left(\frac{t_{fin}}{p_{f_i} - t_{fin}}\right)^{-0.2659} \tag{3.38}$$

For the turbulent region, the Colburn and friction factors are:

$$j_i = 0.2435 \cdot Re_i^{-0.4063} \cdot \left(\frac{p_{f_i} - t_{fin}}{b_i - t_{fin}}\right)^{-0.1037} \cdot \left(\frac{t_{fin}}{\lambda_i}\right)^{0.1955} \cdot \left(\frac{t_{fin}}{p_{f_i} - t_{fin}}\right)^{-0.1733} \tag{3.39}$$

$$f_i = 1.8699 \cdot Re_i^{-0.2993} \cdot \left(\frac{p_{f_i} - t_{fin}}{b_i - t_{fin}}\right)^{-0.0936} \cdot \left(\frac{t_{fin}}{\lambda_i}\right)^{0.682} \cdot \left(\frac{t_{fin}}{p_{f_i} - t_{fin}}\right)^{-0.2423} \tag{3.40}$$

To see whether the fluid flow is laminar or turbulent, the Reynolds number needs to be determined:

$$Re_i = \frac{G_i \cdot D_{h_i}}{\mu_i} \tag{3.41}$$

Where G_i is the mass velocity and D_{h_i} is the hydraulic diameter. The mass velocity and hydraulic diameter are defined by:

$$G_i = \frac{\dot{m}_i}{A_{c_i}} \tag{3.42}$$

$$D_{h_1} = \frac{4 \cdot A_{c_1} \cdot L_{HX}}{A_{t_1}} \tag{3.43}$$

$$D_{h_2} = \frac{4 \cdot A_{c_2} \cdot W_{HX}}{A_{t_2}} \tag{3.44}$$

It was found that the experimental data that Manglik and Berglis obtained [15] did not indicate the typical sudden shift associated with the transition from laminar to turbulent flow. Instead, the friction factor (f) and Colburn (j) vary smoothly and continuously with the Reynolds number (Re). This finding implied that the data may be effectively explained by a single equation that includes the laminar, transition, and turbulent zones [15]. Manglik and Berglis then devised an equation for the friction and Colburn factor that takes into account these regions, which is shown in equations 3.45 and 3.46:

$$j_{i,a} = 0.6522 \cdot Re_i^{-0.5403} \cdot \left(\frac{p_{f_i} - t_{fin}}{b_i - t_{fin}}\right)^{-0.1541} \cdot \left(\frac{t_{fin}}{\lambda_i}\right)^{0.1499} \cdot \left(\frac{t_{fin}}{p_{f_i} - t_{fin}}\right)^{-0.0678}$$

$$j_{i,b} = \left[1 + 5.269 \cdot 10^{-5} \cdot Re_i^{1.34} \cdot \left(\frac{p_{f_i} - t_{fin}}{b_i - t_{fin}}\right)^{0.504} \cdot \left(\frac{t_{fin}}{\lambda_i}\right)^{0.456} \cdot \left(\frac{t_{fin}}{p_{f_i} - t_{fin}}\right)^{-1.055}\right]^{0.1}$$

$$j_i = j_{i,a} \cdot j_{i,b} \tag{3.45}$$

$$f_{i,a} = 9.6243 \cdot Re_i^{-0.7422} \cdot \left(\frac{p_{f_i} - t_{fin}}{b_i - t_{fin}}\right)^{-0.1856} \cdot \left(\frac{t_{fin}}{\lambda_i}\right)^{0.3053} \cdot \left(\frac{t_{fin}}{p_{f_i} - t_{fin}}\right)^{-0.2659}$$

$$f_{i,b} = \left[1 + 7.669 \cdot 10^{-8} \cdot Re_i^{4.429} \cdot \left(\frac{p_{f_i} - t_{fin}}{b_i - t_{fin}}\right)^{0.92} \cdot \left(\frac{t_{fin}}{\lambda_i}\right)^{3.767} \cdot \left(\frac{t_{fin}}{p_{f_i} - t_{fin}}\right)^{0.236}\right]^{0.1}$$

$$f_i = f_{i,a} \cdot f_{i,b} \tag{3.46}$$

With these variables determined, the heat transfer coefficient [16] can be calculated:

$$h_{c,i} = \frac{j_i \cdot G_i \cdot C_{p,i}}{Pr_i^{2/3}} \tag{3.47}$$

Where Pr_i is the Prandtl number of the fluid.

Overall Heat Transfer Coefficient

With the heat transfer coefficient of each fluid determined, it is now possible to determine the overall heat transfer coefficient [16, 17]. This term is defined by equation 3.48:

$$\begin{gathered} \frac{1}{UA_i} = \frac{1}{\eta_{o_i} \cdot h_{c,i} \cdot A_{t_i}} \\ UA = \frac{1}{1/UA_1 + 1/R_w + 1/UA_2} \end{gathered} \tag{3.48}$$

Where η_{o_i} is the overall surface (fin) efficiency, A_i is the total surface area at which the heat exchange occurs, and R_w is the thermal resistance [16, 17]. To define η_{o_i}, the single fin efficiency needs to be computed first:

$$\eta_{f_i} = \frac{tanh(m_i \cdot L_{f_i})}{m_i \cdot L_{f_i}} \tag{3.49}$$

Where the fin length (L_{f_i}) and the m value are defined by:

$$L_{f_i} = \frac{b_i}{2} - t_{fin} \tag{3.50}$$

$$m_i = \sqrt{\frac{2 \cdot h_{c,i}}{k_{al} \cdot t_{fin}} \cdot \left(1 + \frac{t_{fin}}{\lambda_i}\right)} \tag{3.51}$$

With the single fin efficiency determined, the overall surface (fin) efficiency can now be calculated:

$$\eta_{o_i} = 1 - (1 - \eta_{f_i} \cdot L_{f_i}) \cdot \frac{A_{f_i}}{A_{t_i}} \tag{3.52}$$

The thermal resistance is calculated by equation 3.53:

$$R_w = \frac{k_{al} \cdot A_w}{t_{plate}} \tag{3.53}$$

Where k_{al} is the thermal conductivity of the heat exchanger material (which in this case is aluminium), and A_w is the conduction area for wall resistance. The conduction area is defined as:

$$A_w = 2 \cdot W_{HX} \cdot L_{HX} \cdot (N_p + 1) \tag{3.54}$$

Effectiveness - NTU Method

The method used to determine the heat transfer is the effectiveness - NTU method [18, 19]. NTU stands for 'Number of Transfer Units', a term used to indicate the general size of heat exchangers. This term (N) is defined as:

$$N = \frac{UA}{C_{min}} \tag{3.55}$$

Where $C_{min} (= \dot{m} \cdot c)$ is the minimum heat transfer capacity rate. The effectiveness of the heat exchanger is defined [19] as the ratio between the actual heat transfer (q) and the maximum heat transfer possible (q_{max}). The heat transfer, q, can be determined by calculating the lost energy from the hot fluid or calculating the cold fluid's gained energy. The equation for q is:

$$q = \dot{m}_h \cdot c_h \cdot (T_{h_1} - T_{h_2}) = \dot{m}_c \cdot c_c \cdot (T_{c_2} - T_{c_1}) \tag{3.56}$$

The maximum heat transfer occurs at the inlet for the hot and cold fluids as that is the region where the maximum temperature difference is [18]. The fluid with the lower C_{min} will undergo this temperature difference to balance the energy lost and gained by both fluids (as shown in equation 3.56). This maximum heat transfer is defined as:

$$q_{max} = (\dot{m} \cdot c)_{min} \cdot (T_{h_{inlet}} - T_{c_{inlet}}) = C_{min} \cdot (T_{h_{inlet}} - T_{c_{inlet}}) \tag{3.57}$$

Looking back at the definition of the heat exchanger effectiveness, the equation is interchangeable depending on which fluid has the lower heat capacity rate, so a general formula was derived [18] based on the type of flow between the two fluids. The effectiveness for cross-flow is defined in equation 3.58:

$$E = 1 - e^{\left[\frac{e^{(-N \cdot C_{ratio} \cdot n)} - 1}{C_{ratio} \cdot n}\right]} \tag{3.58}$$

Where:

$$C_{ratio} = \frac{C_{min}}{C_{max}} \quad , \quad n = N^{-0.22} \tag{3.59}$$

The equations used to determine the exit temperatures and the heat transfer if the minimum heat capacity rate is for the cold or hot fluid, respectively, in cross-flow conditions, are:

$$T_{c_2} = T_{c_1} + E \cdot (T_{h_1} - T_{c_1}) \rightarrow T_{h_2} = T_{h_1} - \frac{q}{m_h \cdot c_h} \tag{3.60}$$

$$T_{h_2} = T_{h_1} - E \cdot (T_{h_1} - T_{c_1}) \rightarrow T_{c_2} = T_{c_1} + \frac{q}{m_c \cdot c_c} \tag{3.61}$$

Pressure Drop

With the heat transfer completed, the pressure drop due to the heat exchanger can be determined. This is done by first identifying the components of the pressure drop and where it occurs, defining the contraction and expansion factors, and finally computing the actual pressure drop using these factors.

Pressure Drop Components

Initially, the incoming flow is assumed to be uniform [12], but as it enters the passageway, it compresses owing to changes in the free-flow region. This causes flow separation at the entry, which is followed by irreversible free expansion. The fluid within the core undergoes skin friction and may also meet form drag at the leading and trailing edges of interrupted fin surfaces [12].

Internal contractions and expansions can occur within the core in some cases, such as in a perforated fin core. When the body heats or cools, the fluid density and mean velocity vary along the flow length. As a result, depending on whether the fluid is being heated or cooled, the fluid within the flow path either accelerates or decelerates [12, 13]. At the core exit, flow separation occurs again, followed by expansion due to changes in the free-flow area. A schematic of the pressure drop components on one side of the heat exchanger can be seen in figure 3.5:

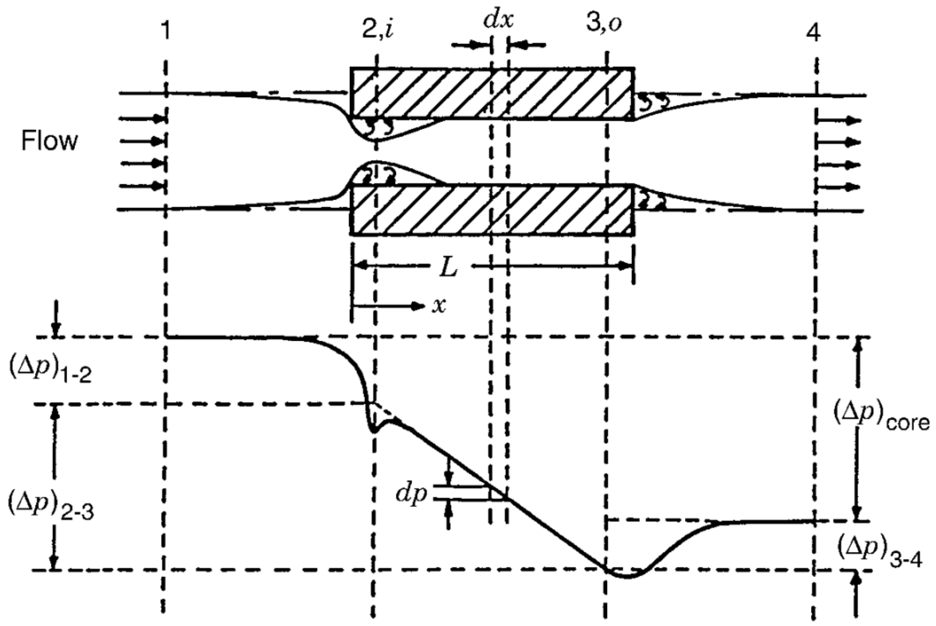

Figure 3.5: Pressure drop components associated with one passage of a heat exchanger, obtained from Shah et al. [12]

The pressure drop on one side of the heat exchanger is denoted by equation 3.62:

$$\Delta p = \Delta p_{1-2} + \Delta p_{2-3} - \Delta p_{3-4} \tag{3.62}$$

As shown in figure 3.5, the subscripts 1, 2, 3, and 4 represent distinct locations: far upstream, passage entry, passage exit, and far downstream. The pressure drop at the core entry caused by abrupt contraction is marked by Δp_{1-2}, the pressure decrease within the core (referred to as the core pressure drop) by Δp_{2-3}, and the pressure increase at the core exit by Δp_{3-4}. Δp_{2-3} is typically the most responsible for the total pressure drop.

Contraction & Expansion Ratio

Before calculating the pressure drop, defining the contraction loss (K_c) and expansion loss (K_e) coefficient for each fluid is necessary. Using figure 3.6, the values of these coefficients can be estimated. In addition, a set of equations was derived by Kays and Londen [20] that calculates the coefficients. The first step is defining the jet contraction ratio for the square-tube geometry:

$$C_{c,tube,i} = 4.374 \cdot 10^{-4} \cdot \left(e^{6.737 \cdot \sqrt{\sigma_i}}\right) + 0.621 \tag{3.63}$$

Where the porosity (σ_i) is defined by the ratio of the free-flow area and frontal area:

$$\sigma_i = \frac{A_{c_i}}{A_{fr_i}} \tag{3.64}$$

The velocity-distribution coefficient for circular tubes is:

$$K_{d,tube,i} = \begin{cases} 1.09068 \cdot (4 \cdot f_{d,i}) + 0.05884 \cdot \sqrt{4 \cdot f_{d,i}} + 1, & \text{if } Re_i \geq 2300 \\ 1.33, & \text{Otherwise} \end{cases} \tag{3.65}$$

Where the friction factor for this geometry is defined as:

$$f_{d,i} = \begin{cases} 0.049 \cdot Re_i^{-0.2}, & \text{if } Re_i \geq 2300 \\ \frac{16}{Re_i}, & \text{Otherwise} \end{cases} \tag{3.66}$$

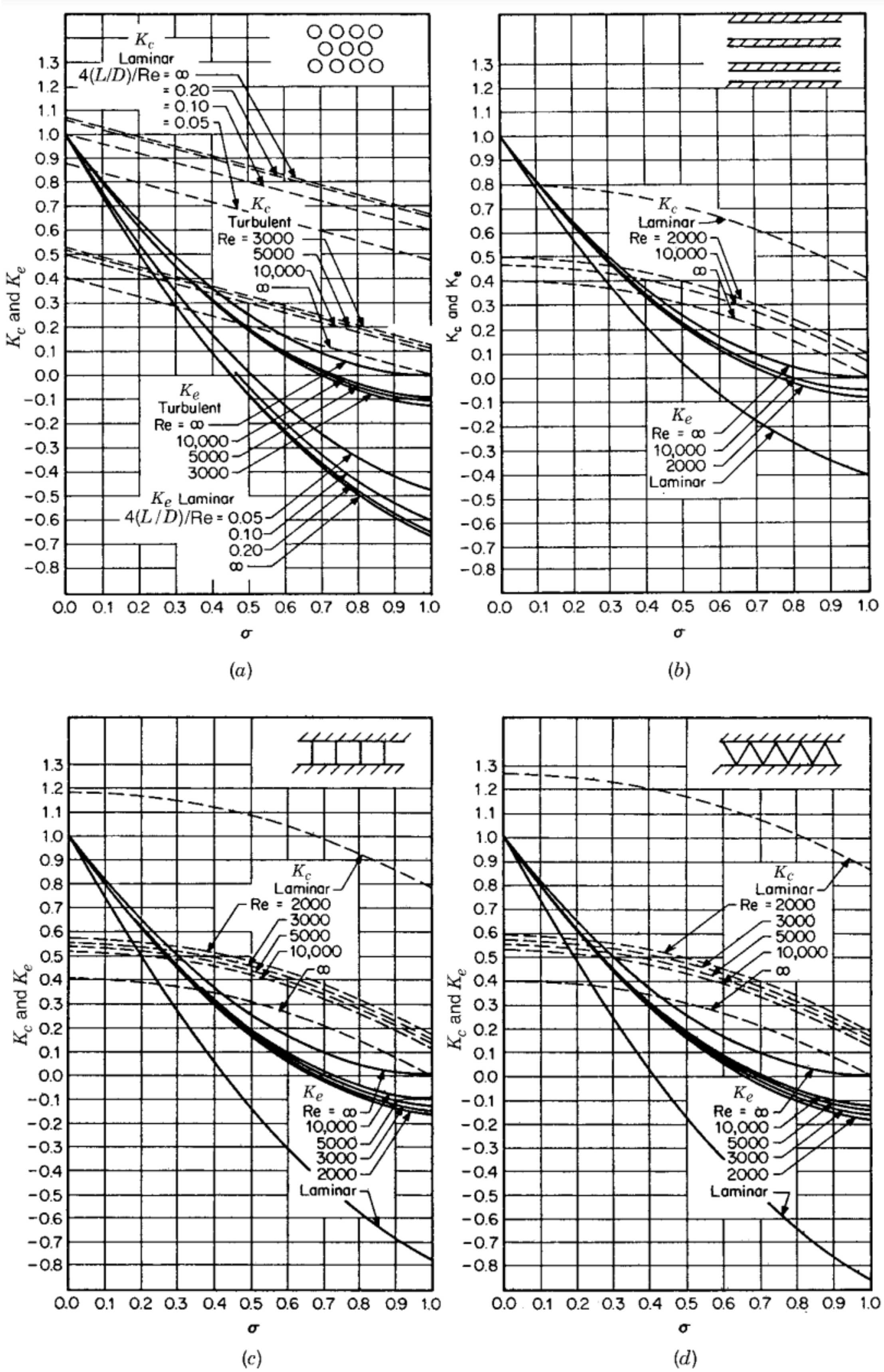

Figure 3.6: Entrance and exit pressure loss coefficients for (a) multiple circular tube core, (b) multiple-tube flat-tube core, (c) multiple square tube core, and (d) multiple triangular tube core with abrupt contraction (entrance) and expansion (exit) [16]

Converting the circular tubes to the square tubes gives:

$$K_{d,square,i} = \begin{cases} 1 + 1.17 \cdot (K_{d,tube,i} - 1), & \text{if } Re_i \geq 2300 \\ 1.39, & \text{Otherwise} \end{cases} \tag{3.67}$$

With these variables determined, the contraction and expansion coefficients can now be computed:

$$K_{c,i} = \frac{1 - 2 \cdot C_{c,tube,i} + C_{c,tube,i}^2 \cdot (2 \cdot K_{d,square,i} - 1)}{C_{c,tube,i}^2} \tag{3.68}$$

$$K_{e_i} = 1 - K_{d,square,i} \cdot \sigma_i + \sigma_i^2 \tag{3.69}$$

Pressure Drop Calculation

With the contraction and expansion coefficients defined, the pressure drop for the plate-fin heat exchanger can now be computed (Which is divided into several parts):

$$\Delta P1_{12} = \frac{G_1^2}{2\rho_{1,in}} \cdot \left(1 - \sigma_1^2 + K_{c_1}\right) \tag{3.70}$$

$$\Delta P1_{23} = \frac{G_1^2}{2\rho_{1,in}} \cdot \left[2 \cdot \left(\frac{\rho_{1,in}}{\rho_{1,out}} - 1\right) + \frac{4 \cdot f_1 \cdot L_{HX}}{D_{h,1}} \cdot \left(\frac{\rho_{1,in}}{\rho_{1,m}}\right)\right] \tag{3.71}$$

$$\Delta P1_{34} = \frac{G_1^2}{2\rho_{1,in}} \cdot \left[(1 - \sigma_1^2 - K_{e_1}) \cdot \frac{\rho_{1,in}}{\rho_{1,out}}\right] \tag{3.72}$$

$$\Delta P1 = \Delta P1_{12} + \Delta P1_{23} - \Delta P1_{34} \tag{3.73}$$

Where $\rho_{1,in}$, $\rho_{1,out}$, and $\rho_{1,m}$ are the inlet, outlet, and mean density:

$$\rho_{1,out} = \frac{P_{1,out}}{R \cdot T_{1,out}} \tag{3.74}$$

$$\frac{1}{\rho_{1,m}} = \frac{1}{2} \cdot \left(\frac{1}{\rho_{1,in}} + \frac{1}{\rho_{1,out}}\right) \tag{3.75}$$

Taking the subscript notation of figure 3.1 into account, the heat exchanger outlet pressure, temperature, and density are:

$$T_{c,2} = T_3 \tag{3.76}$$

$$P_{1,out} = P_2 - \Delta P1_{12} = P_3 \tag{3.77}$$

$$\rho_{1,out} = \rho_3 \tag{3.78}$$

3.2.4. Nozzle (Stages 3-4)

Finally, the exhaust nozzle vents the excess heat absorbed by the heat exchanger. Determining the properties will be a similar approach to that taken for the diffuser. When the nozzle outlet properties are resolved, it is possible to calculate the total net force. To calculate the total net force of the engine [11], the following equation is used:

$$F_{net} = \dot{m}_4 \cdot (V_4 - V_1) + A_4 \cdot (P_4 - P_1) - A_1 \cdot (P_1 - P_0) \tag{3.79}$$

This net force is an initial, simplified estimation that does not consider the pressure distribution due to the normal and tangential forces on the inner walls of the diffuser and nozzle.

To determine the amount of drag conserved due to the Meredith effect [1], the duct model can be calculated with no heat transfer (q = 0) occurring at the heat exchanger. The net force can then be computed again and the difference would be compared:

$$\Delta F_{net} = F_{net,c} - F_{net,h} \tag{3.80}$$

3.3. Optimisation Of The Cooling Duct

The numerical tool aims to minimise the drag penalty of the aerodynamic cooling duct while transferring 100% of the heat absorbed by the heat exchanger from the aircraft into the ambient air. This is done by optimising the shape of the duct components (i.e. the inlet diffuser and outlet nozzle), and the sizing and effectiveness of the heat exchanger. The method of optimisation for this project is the Individual Discipline Feasible (IDF) architecture. The disciplines that affect the aerodynamic cooling ducts are; aerodynamics and thermodynamics. However, as these disciplines are interrelated throughout each stage of the duct, it is better to model the disciplines of this optimisation process by the components of the duct which are; the upstream, the diffuser, the heat exchanger and the nozzle.

3.3.1. Disciplines

The ambient properties (Pressure, temperature, density, etc.) and drag profiles (C_D) of the aerodynamic duct will be the main focus of the upstream, diffuser and nozzle disciplines. The geometry of these duct parts, as well as the flight parameters (such as flight altitude, flight speed, etc.), are required as input for these disciplines. These fields will assist in examining the efficacy of different duct designs in reducing the drag penalty.

For the heat exchanger discipline, the preliminary sizing and performance of the heat exchanger are determined using the compact heat exchanger approach. This requires the inlet temperatures ($T_{c,in}$, $T_{h,in}$), mass flows ($\dot{m}_c, \dot{m}_h$) of the hot and cold fluids (i.e. the coolant and the ambient air, respectively), and the effectiveness (E_{HX}) of the heat exchanger, which can be estimated using the NTU-method. The outcome of this discipline will be the geometric properties of the heat exchanger, the outlet temperatures of the hot and cold fluids, and the total heat transfer (Q_{total}).

These disciplines will also analyse the preliminary sizing of the duct components and determine the overall weight by using the cooling duct and aircraft specifications as input. Calculating this increase will determine how much fuel or payload weight can be stored (assuming the max take-off weight cannot be altered) which will affect the propulsive and performance properties. This will help determine whether the designs of the ducts outweigh the drawbacks (i.e. reduction in fuel weight or payload).

3.3.2. Objective Function, Design Vector & Constraints

The objective function is the internal drag profile (C_D) of the duct as the aim of this assignment is to minimise this value. This is the negative value of the net force which was shown in equation (3.79):

$$f(x) = C_D(x) = -F_{net}(x) \tag{3.81}$$

Where x is the design vector which contains all of the required inputs. Constraints and bounds are used to discard some of the unfeasible solutions. The design vector for this optimisation process includes the specifications of the duct and the specifications of the heat exchanger. Although the specifications of the aircraft and the flight conditions are required inputs as well, these values are constant throughout the optimisation process. For this reason, these inputs are not included in the full design vector. Taking these factors into account, the full design vector is:

$$x = \left[\frac{W_{HX}}{L_{HX}}, \frac{A_1}{A_2}, \frac{A_4}{A_3}\right] \tag{3.82}$$

The bounds for the design vector are:

Table 3.1: Upper and lower bounds of the design vector

Design variable	Initial value	Lower bound	Upper bound
W_{HX}/L_{HX}	1.0	1/5	5.0
A_1/A_2	1/1.8	1/5	1.0
A_4/A_3	1/1.8	1/5	1.0

When considering the disciplines and how they interact, the constraints that should be imposed are the structural constraints. The mass gain should be minimal so that the maximum fuel weight (W_f) can be retained. Taking that into account, an example of a constraint can be that the duct weight is less than 20% of the fuel weight:

$$g(x) = W_{duct} \leq 0.2 \cdot W_f \tag{3.83}$$

These constraints are used to ensure that the design of the ducts does not greatly impact the performance of the aircraft negatively. It will also be more refined (alongside the design vector and bounds) during the literature study and the construction of the numerical tool.

3.3.3. IDF Architecture

The IDF architecture is presented as an XDSM diagram. This is shown in figure 3.7. The number 0 to 8 in the XDSM diagram indicates the operation sequence. Starting with 0, the initial values are passed to the optimiser. In 1, the optimiser passes these values to the four disciplines indicated in the green box in steps 2 to 5. Each discipline is sequentially dependent and their results influence each other.

The results from these four disciplines are used in step 6, where the converged values are used to determine the value of the objective function and check whether the design constraints are met. The objective function and constraints only take in the necessary input values.

If the constraints are not met, the output shown in step 8 is fed back to the optimiser to start a new iteration. Then a new set of input values is given to the four disciplines to carry on the operation. If all constraints are met, the outputs have converged and the optimisation process is completed.

3.4. Preliminary External Analysis Of The Cooling Duct

The focus shifts from internal to external analysis of the duct. The simulation uses the Reynolds Averaged Navier-Stokes equations, a fundamental set of equations in fluid dynamics that are solved using OpenFOAM because of its organised code structure, simplicity, and reliability [21].

The study investigates an axisymmetric duct that releases air into motionless surroundings. The flow's Reynolds number is affected by the flight phase under consideration. The duct is designed with trapezoidal geometries for the diffuser and nozzle, as well as a rectangular box for the heat exchanger. The computational domain, which represents the area under consideration [21], is sufficient in size to predict the behaviour of the airflow far away from the duct.

A preprocessing phase is performed to facilitate the simulation, which involves converting the geometry into a two-dimensional format and constructing a hexagonal mesh. The to-be-constructed geometry of the duct will only consist of the top wall as using the full duct will be seen as a closed system (i.e. the duct inlet and outlet are fixed walls). This is because OpenFOAM does not allow internal faces to be generated. Due to time constraints, a preliminary evaluation of the top wall contour of the duct is made instead.

The geometry and mesh are created using GMSH, a software tool. The resulting computational domain provides the basis for the subsequent numerical analysis, which is shown in figure 3.8:

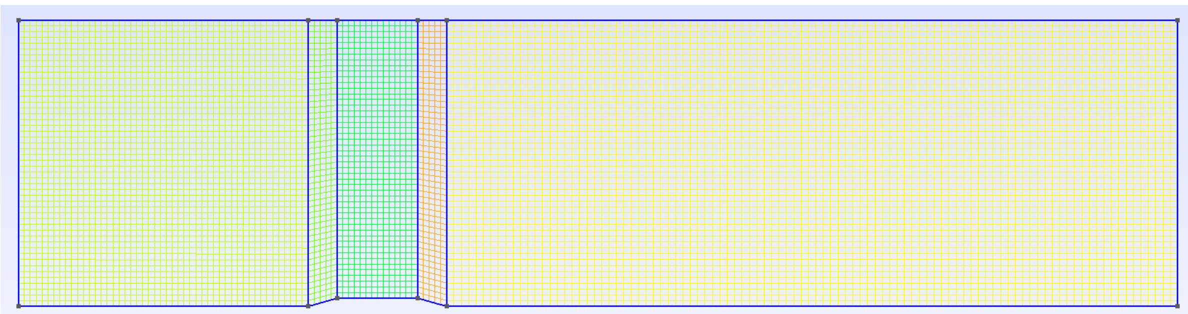

Figure 3.8: Structured mesh of the top wall contour of the cooling duct used with GMSH

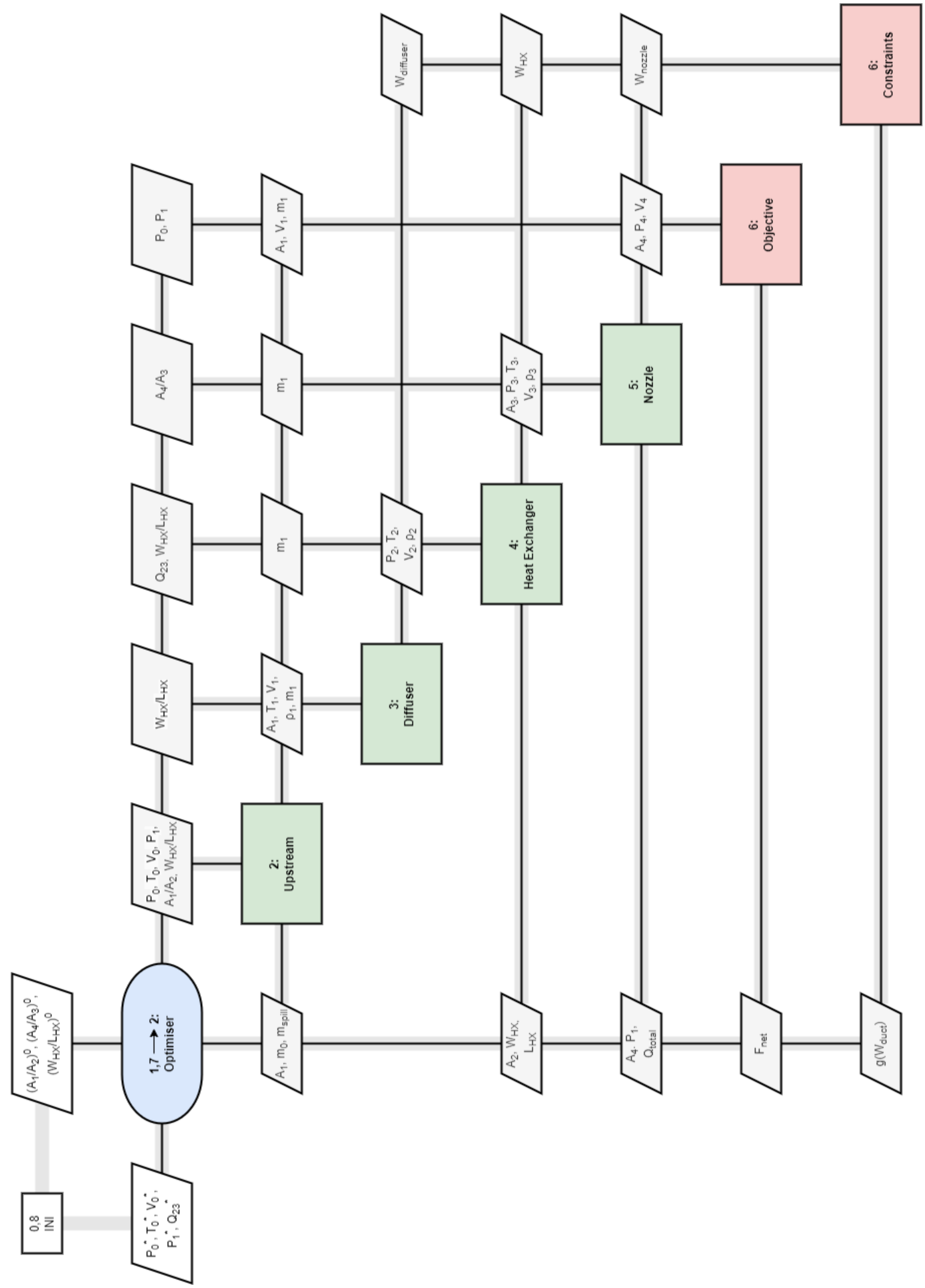

Figure 3.7: XDSM diagram based on the IDF method

Following the identification of the physics of the problem, the fluid characteristics, flow physics model, and boundary conditions need to be defined. This critical stage in computational modelling guarantees that the simulation correctly depicts the real-world event under consideration [21]. One may decide how the fluid behaves inside the computational domain by describing the fluid parameters, specifying the suitable flow physics model, and providing boundary conditions.

The totalPressure boundary condition is established at the domain's inlet in this example to simulate the upstream air conditions. It is assumed that the pressure at the outlet is constant and equal to the ambient surroundings. The zeroGradient Newman boundary condition for temperature is applied to all surfaces except the entrance, which has a constant ambient temperature specified. In terms of velocity, the zeroGradient condition is used at the nozzle's output to indicate no change in velocity, whereas the no-slip condition is utilised on the walls to indicate zero velocity at the wall limits. The simulation is performed in a 3D field using OpenFOAM. However, to simulate a 2D flow, the empty condition is used for all characteristics, essentially limiting the simulation to a two-dimensional environment.

The solution to the set of governing equations is reached in the presented simulation through an iterative process utilising the SIMPLE algorithm [21]. This approach, which is implemented in OpenFOAM as a solver called rhoSimpleFoam, is used to solve fluid flow equations repeatedly.

A convergence criterion is used to verify accuracy. For global residuals, a convergence level of 10e-6 is established in this work. Achieving a high level of convergence is critical because it implies that the numerical solution has stabilised and attained a consistent state. However, without validation of the results, it is uncertain whether the data obtained from the simulation is reliable and accurate.

3.5. Analysis At The Aircraft System Level

This section discusses the methodology used to test the effect the numerical tool has on the Dash 8-300 as a whole system. The specifications of the aircraft can be seen in table 3.2:

Table 3.2: Dash 8-300 list of specifications, obtained from aircraft data [22]

Variable	Value
Wing span	27.4 m
Wing surface area	56.2 m^2
Max take-off weight	19,505 kg
Operative empty weight	11,793 kg
Max fuel weight	2,559.6 kg
Max power output	1,860 kW
Cruise speed	532 km/h
Range	1,711 km

In addition, an in-depth analysis of the flight profile will be carried out to see how the aircraft performs during each flight phase (from take-off to landing). The flight profile analysis is carried out and presented in chapter 5. The flight profile of the use case can be seen in figure 3.9:

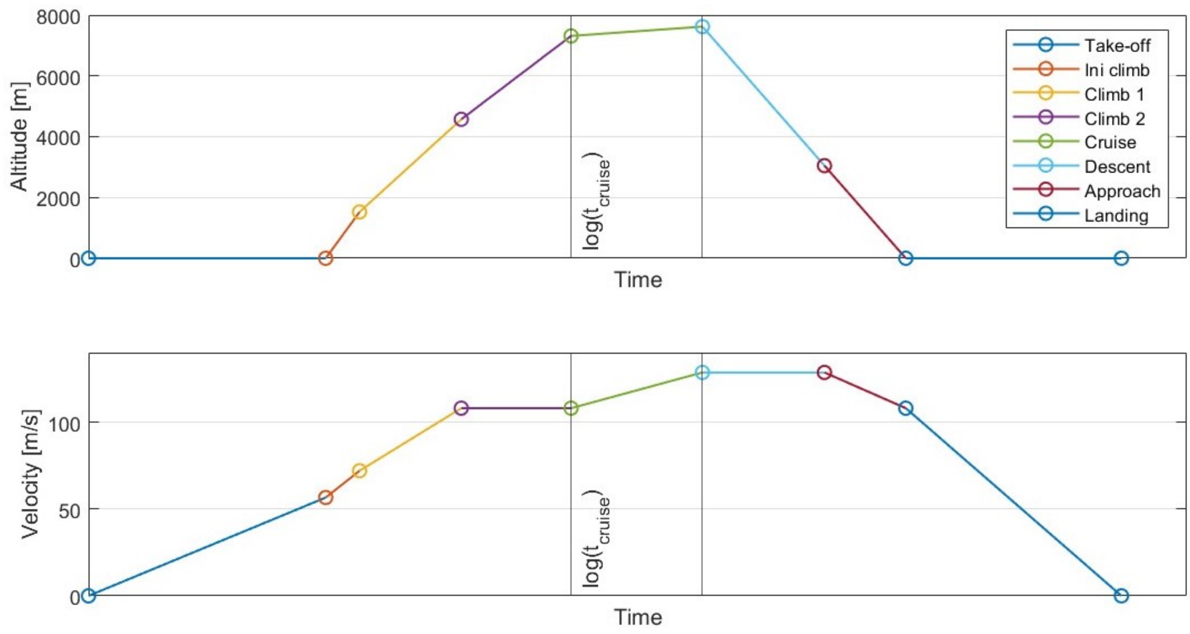

Figure 3.9: De Havilland Canada Dash 8-300 flight profile obtained from aircraft data [23]

3.5.1. Payload-Range Analysis Of The Aircraft System

The focus of this performance analysis is to create a payload-range diagram. This will analyse the trade-off between the passenger payload and range [24] of the aircraft for both the standard configuration and the fuel cell/duct configuration. For this tool, the aircraft that will be analysed is the Dash 8-300. An example of this diagram can be seen in figure 3.10:

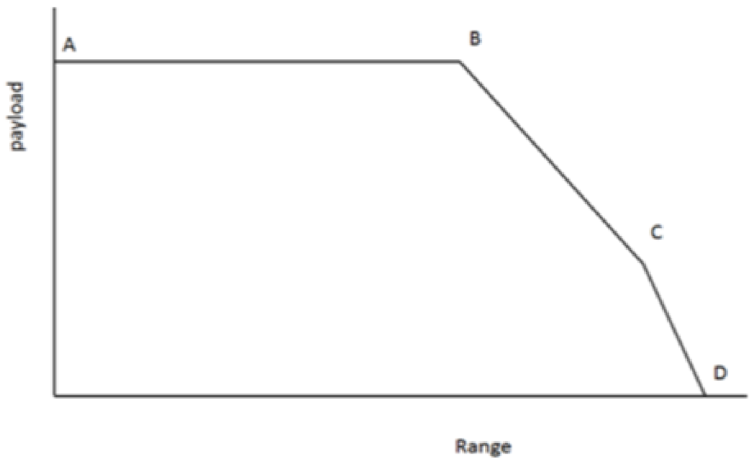

Figure 3.10: Example of a payload-range diagram

The diagram consists of four main stages:

1. Point A: Max payload at zero range (W_p=$W_{p,max}$, R=0)
2. Point B: Max payload at design range (W_p=$W_{p,max}$, R=R_{des})
3. Point C: Payload and range at max fuel weight (W_f = $W_{f,max}$)
4. Point D: Max range at zero payload and max fuel weight (W_p=0, W_f = $W_{f,max}$)

To determine the range [24] of an aircraft, the following equation (3.84) is used:

$$R = \left(\frac{\eta_p}{g \cdot c_p}\right) \cdot \left(\frac{L}{D}\right)_{cruise} \cdot ln\left(\frac{W_{start}}{W_{end}}\right) \tag{3.84}$$

Where η_p is the propeller efficiency, c_p is the power specific fuel consumption (PSFC), $(L/D)_{cruise}$ is the lift-to-drag ratio at cruise, and W_{start}/W_{end} is the weight ratio before and after cruise.

The assumptions that were used when constructing the payload range diagrams for both the standard configuration and fuel cell configuration are:

- The flight phase fuel fractions are assumed based on the literature on regional turboprops [25].
- The lift-drag ratio is calculated based on the weight of the aircraft during cruise and the amount of thrust required to maintain that cruise speed.
- The reserve fuel weight fraction for the standard and fuel cell configurations is 0.1.
- The passenger weight is assumed to be 95 kg (without cargo) based on literature [26].
- The fuel tank for the fuel cell configuration is modelled the same as that of the kerosene configuration.
- The H2 flight phase fuel fractions are scaled based on the ratio of kerosene to H2 LHVs (Lower heating values).

For this case, it is assumed that η_p is 0.3 [27] and, from literature [28], c_p is 0.564 kg/kWh. For the lift-to-drag ratio, it is assumed that the aircraft is flying in a steady, symmetric flight (i.e., thrust is equal to drag and weight is equal to lift). At cruise, the power setting is assumed to be 80% of the maximum power output. With this value and the aircraft's cruise speed (obtained from literature [27]), the thrust of the aircraft can be determined:

$$F_{cruise} = \frac{P_{cruise}}{V_{cruise}} \tag{3.85}$$

To determine the start weight, the passenger payload weight and fuel weight for each stage need to be determined. The passenger payload weight is the number of passengers multiplied by the average passenger weight (95 kg from literature [26]):

$$W_{p,pax} = n_{pax} \cdot W_{pax} = 95 \cdot n_{pax} \tag{3.86}$$

The cargo weight of the passengers is determined by calculating the difference between the passenger payload weight and the maximum payload weight:

$$W_{p,cargo} = W_{p,max} - W_{p,pax} \tag{3.87}$$

For the conventional aircraft, a reserve fuel fraction ($f_{reserve}$) of 10% is taken into account. Depending on the stage, the fuel weight is multiplied by a factor of 0.9.

$$W_f = \begin{cases} (MTOW - OEW - W_{p,max}) \cdot (1 - f_{reserve}) & \text{Point B} \\ W_{f,max} \cdot (1 - f_{reserve}) & \text{Point C \& D} \end{cases} \tag{3.88}$$

Since this case focuses on the passenger payload range, the cargo weight is neglected in the determination of the start weight (W_{start}). Therefore, the difference in weight (i.e., W_{diff}) is calculated with equation 3.89:

$$W_{diff} = MTOW - OEW - W_f - W_{f,reserve} - W_{p,pax} \tag{3.89}$$

The start weight is determined by multiplying the difference between maximum take-off weight (MTOW) and the difference weight (W_{diff}) with the typical fuel fractions of the non-intensive flight phases before cruise (i.e., from engine startup to climb):

$$W_{start} = (MTOW - W_{diff}) \cdot f_{startup} \cdot f_{taxi} \cdot f_{TO} \cdot f_{climb} \tag{3.90}$$

Where f_i is the phase fuel fraction, which is obtained from the literature of typical regional turboprops [25]:

Table 3.3: Non-intensive fuel fractions of regional turboprop aircraft

Flight Phase	Fuel Fraction [-]
Start-up	0.995
Take-off	0.995
Climb	0.985
Cruise	0.918
Descent	0.985
Land	0.995

The end weight is the difference between the start weight and the fuel weight used during cruise:

$$W_{end} = W_{start} - W_f \tag{3.91}$$

With all the terms derived, the range can now be calculated for each stage.

When considering the duct, the lift-drag ratio needs to be redefined by including the internal net force and external drag. This value considers the total drag produced by two cooling ducts, one for each wing. Depending on the configuration, the duct mass needs to be deducted from either the fuel weight, payload, or a combination of both. This is done to conserve the maximum take-off weight (MTOW). As the focus is on the effect of the cooling duct, it is assumed that the fuel tanks for the fuel cell configuration are the same as those for the kerosene configuration. This is further discussed in chapter 6.

In reality, switching the conventional aircraft to the H2 configuration has a direct effect on the operational empty weight due to the replacement of the kerosene fuel tanks with H2 fuel tanks. In addition, the propulsion system requires a new set of components. These new components are [27]: replacing the turboprop powerplants with an electromotor; adding a fuel cell stack system; and including a new electronic control system. Also, switching the fuel source has a direct effect on the propulsive properties, namely the PSFC (C_p). For fuel cell propulsion, it is assumed that the scaling of the PSFC is between the electric chain efficiencies of the system for direct combustion [27]. However, for the scope of this project, it is assumed that these effects do not apply, as the focus is on the effects of the cooling ducts on the aircraft system specifically.

3.5.2. Performance Diagrams Of The Aircraft System

Another way of evaluating the performance of the aircraft with cooling ducts is to analyse the change in power loading and wing loading. This is done to see if the addition of the cooling ducts produces a better overall design point. The first step to constructing the performance diagram is to determine the sizing of the wing loading for stall speed. This is determined using the following equation:

$$\left(\frac{W}{S}\right)_s = \frac{1}{2} \cdot \rho_{SL} \cdot V_s^2 \cdot C_{L,max,land} \tag{3.92}$$

Where V_s is the stall speed. This computed value will appear as a vertical line in the diagram and will act as a boundary for the design point. The next step is to determine the take-off parameter (TOP). To calculate the TOP, equation (3.93) is used:

$$\text{TOP} = \left(\frac{W}{S}\right)_{TO} \cdot \left(\frac{W}{P}\right)_{TO} \cdot \frac{1}{C_{L,max,TO}} \tag{3.93}$$

With this formula, a plot can be crafted between W/S and W/P. For the landing phase, the wing loading can be calculated using the following equation:

$$\left(\frac{W}{S}\right)_{ld} = \frac{C_{L,max,ld} \cdot \rho_{SL} \cdot s_{ld}}{2 \cdot f_{ld}} \tag{3.94}$$

Where f_{ld} is the weight ratio for the landing phase, obtained from table 3.3, and s_{ld} is the landing distance. Like the stall phase, this value is represented as a vertical boundary in the diagram. Finally, the cruise performance can be determined. Correcting the formula to 80% throttle and 91.8% of the maximum take-off weight, equation (3.95) is used to plot the cruise requirement:

$$\left(\frac{W}{P}\right)_{cr} = 0.8 \cdot \eta_p \cdot \left(\frac{\rho_{cr}}{\rho_{SL}}\right)^{0.75} \cdot \left[\frac{C_{D_0} \cdot 0.5 \cdot \rho_{cr} \cdot V_{cr}^3}{0.918 \cdot W/S} + \frac{0.8 \cdot W/S}{\pi \cdot A \cdot e \cdot 0.5 \cdot \rho_{cr} \cdot V_{cr}}\right]^{-1} \tag{3.95}$$

Where V_{cr} and ρ_{cr} are the flight speed and density at cruise, C_{D_0} is the zero-lift drag coefficient, A is the aircraft wing aspect ratio, and e is the Oswald efficiency.

Constructing the performance diagram will aid in assessing and comparing the performance of the aircraft configurations with and without cooling ducts. With a visual representation of the distribution of aircraft weight and power across various flight conditions, one can gain a comprehensive understanding of the system's performance characteristics. By evaluating the power loading and wing loading values at different operating points, an assessment can be made regarding the aerodynamic and propulsive efficiencies of each configuration. This insight is instrumental in optimising the relationship between thrust, weight, and wing area to meet or improve specific operational requirements. The differences in the performance diagram between the conventional and duct configurations are discussed in chapter 6.

Finally, propulsive properties such as fuel flow and specific fuel consumption are evaluated across various flight phases. By examining these values, one can observe the impact of cooling ducts on the overall energy requirements of the aircraft. For the fuel weight used per phase, the following equation is used:

$$W_f = MTOW - W_{i-1} \cdot f_i \tag{3.96}$$

Where W_i is the flight phase weight and f_i is the flight phase fuel fraction. The fuel fractions for the flight phases are the same as those in table 3.3. After determining how much fuel is used during each flight phase, the fuel flow for both configurations can be determined with equation 3.97:

$$\dot{m}_f = \frac{W_f}{t_i} \tag{3.97}$$

Where t_i is the duration of each flight phase. This is determined by using equation 3.98:

$$t_i = \begin{cases} \frac{d}{V} & \dot{\gamma} = 0 \\ \frac{h}{\text{RoC}} & \dot{\gamma} \neq 0 \end{cases} \tag{3.98}$$

Where d is the horizontal distance and $\dot{\gamma}$ is the rate of climb. The specific fuel consumption (SFC) can now be calculated as the ratio of the fuel flow and the total thrust produced by each configuration:

$$\text{SFC} = \frac{\dot{m}_f}{T_{AC}} \quad , \quad \text{SFC}_{Duct} = \frac{\dot{m}_f}{T_{AC} + F_{net}} \tag{3.99}$$

Where T_{duct} is the net force of the duct and T_{AC} is the thrust of the aircraft in standard configuration. T_{AC} is determined as the ratio of the available power of the aircraft in a certain phase to the respective flight velocity:

$$T_{AC,i} = \frac{P_{a,i}}{V_i} \tag{3.100}$$

Like the payload-range diagram, the propulsive properties differ depending on the configuration setup, as they will have differing fuel weights, payload weights, or a combination of both. This is further discussed in chapter 6.

4

Verification & Validation

In this chapter, the verification and validation procedures are presented.

4.1. Verification

After creating a numerical model, it should be evaluated to ensure that it truly does the task at hand. There are two aspects to the verification strategy: code verification and computational verification.

4.1.1. Code Verification

The goal of code verification is to ensure that the code works properly and completes all required objectives. The actual writing of the code is the main emphasis of this verification section. As a result, testing the code entails looking for flaws in syntax or code assembly. The approach for verifying the code follows the outline shown below:

1. **Syntax Check:** The program will not execute if there are simple syntax problems. The interpreter or compiler will display error or warning messages, allowing the programmer to rapidly identify and remedy the fault.
2. **Output Check:** The program will take a set of inputs and generate certain outputs, perhaps in a long sequence of phases. The use of print statements is the simplest technique to ensure that the code is executing all jobs appropriately. If the input data is not yet available, test data might be used instead. The print statements allow you to track the program's execution at each stage and see if the results are as intended.
3. **Visualisation Check:** When the quantity of data to be handled is vast, verifying the code using print statements can be time-consuming, especially when the pattern is given by a sequence of integers. As a last phase, or to assist in the preceding process, visualisation tools such as graphs are used. By evaluating crucial parts of a curve, such as checking if the outlet pressure and ambient pressure are identical, one may rapidly determine if the code's results are truly appropriate.

4.1.2. Computational Verification

After the syntax has been verified, the code must be tested to ensure that it achieves what was intended. This is best accomplished by testing discrete pieces of code, known as units. Because units are easier to grasp, errors can be detected more quickly. Different units may also generate mistakes that cancel out in the scenario at hand but not in others.

The diffuser and nozzle are modelled as simple shapes in quasi-1D flow. These functions can be verified by inputting examples of flight conditions in the function and calculating the output by hand to check whether the answers are identical.

The heat exchanger is modelled using the compact heat exchanger design approach and the effectiveness - NTU method. To verify that the calculations are correct, the values can be compared to literature data [16]. The inputs and outputs of the heat exchanger verification can be seen in tables 4.1 and 4.2:

Variable	Value	Unit
Inlet temperature 1	1173.15	K
Inlet temperature 2	473.15	K
Inlet pressure 1	160	kPa
Inlet pressure 2	200	kPa
HX width	0.303	m
HX length	0.303	m
HX height	0.948	m
Fin thickness	0.102	mm
Plate thickness	0.5	mm
Fin density	782	1/m
Spacing between plates	2.49	mm
Offset strip length	3.175	mm
Thermal conductivity	18	W/mK

Table 4.1: Heat exchanger model inputs, obtained from Kakac et al. [16]

Variable	Ref model	Current model	Difference [%]
Outlet temperature 1 [K]	596.35	596.354	0.00057
Outlet temperature 2 [K]	975.634	975.631	0.000287
Pressure difference 1 [kPa]	10.004	10.005	0.009996
Pressure difference 2 [kPa]	7.784	7.787	0.0385
NTU [-]	7.134	7.133	0.0126
HX Effectiveness [-]	0.824	0.824	0.0
HX Heat transfer [mW]	1.078	1.0782	0.01855

Table 4.2: Verification of the heat exchanger model outputs, obtained from Kakac et al. [16]

From the comparison of the two sets of outputs, it can be seen that the heat exchanger model is functional (i.e., no negligible differences/errors) and produces the correct outputs.

4.2. Validation

The goal of numerical model validation is to guarantee that simulations properly replicate real-world events or physical processes. To validate the numerical model, one needs to analyse data from other sources as it ensures the correctness and dependability of the numerical findings.

4.2.1. Comparison

The first validation source was investigated by L. Piancastelli and M. Pellegrini [7]. In their paper, they investigated the Meredith effect by applying a cooling duct to a VD007 hybrid turbo-diesel engine. The second validation source is a continuation of this research [8], as L. Piancastelli, alongside L. Frizziero and G. Donicci, looked into improving the Meredith effect on piston engine cooling in terms of placement and temperature limits. These sources are expanded in section 2.4.

To compare their results with the numerical model, the inputs for the numerical data are identical to the recorded inputs from the papers. Assuming that the control volume encompasses the interior of the cooling duct and the flight conditions are set at 8570.4 m and 231.1 m/s for data set 1, and 5000 m and 152.9 m/s for data set 2, the comparison of the outputs of the two data sets can be seen in figures 4.1 and 4.2:

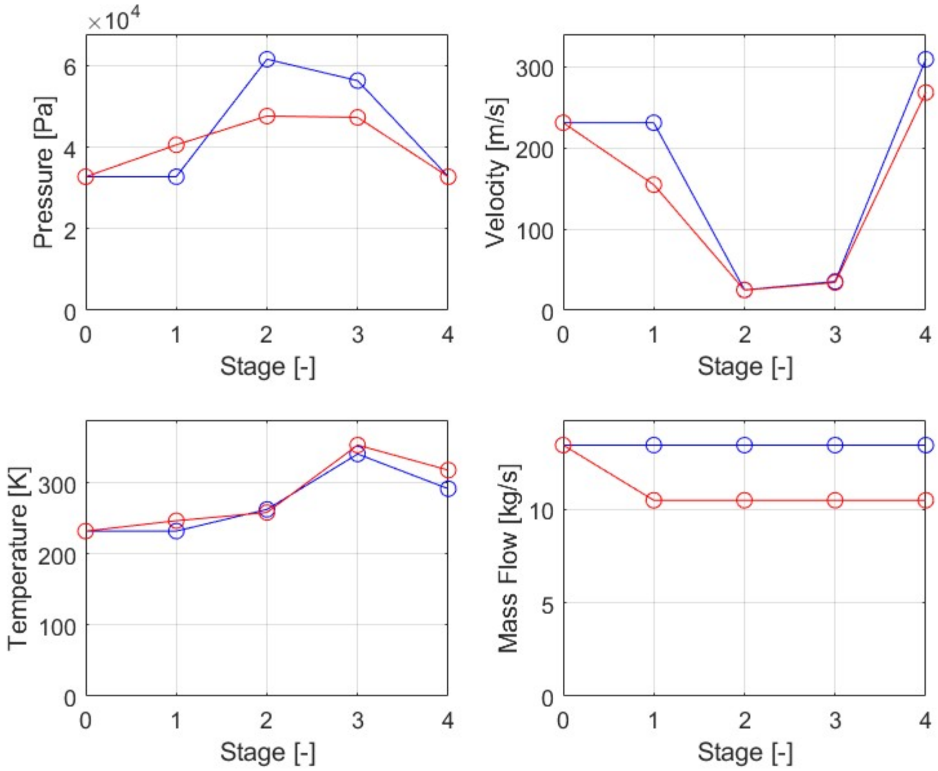

Figure 4.1: Comparison of numerical model (Red) and validation source (Blue) from Piancastelli et al. [7]

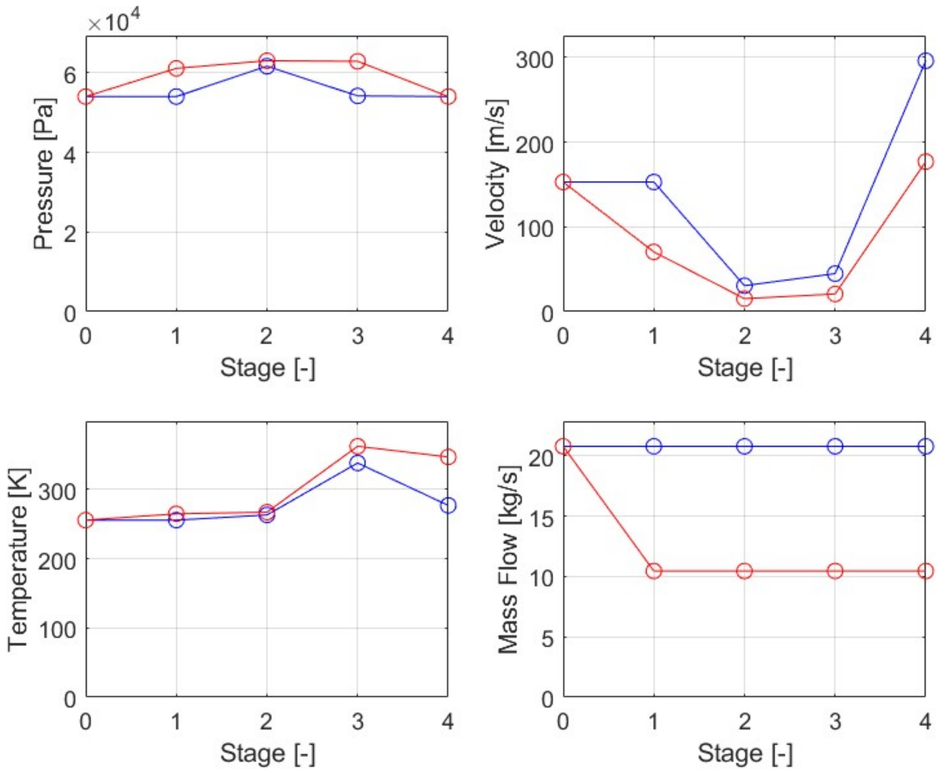

Figure 4.2: Comparison of numerical model (Red) and validation source (Blue) from Piancastelli et al. [8]

Based on the first graph, there is quite a large difference in pressure distribution (16.01-23.86%), except for stage 4. In addition, there is little change in the temperature (1.63-8.99%) and velocity (0.89-3.54%) distributions, except for stage 1. Also, the internal mass flow differed since no mass flow spill is seen in the reference data.

Looking at the second graph, there is a small/moderate difference in pressure distribution (2.24-16.02%) and little temperature change (except for stage 4) distribution (1.53-7.13%). There is also a large difference in velocity distribution at stages 1 and 4 (40.2-53.93%) and, like the first graph, there is a mass flow difference due to the zero mass flow spill.

The causes of these differences could likely be due to a difference in the assumptions made during the calculations. For example, the reference model assumes no change between stages 0 and 1 (i.e., no mass flow spill), whereas the numerical model does. Another potential cause is that small differences exist in the heat exchanger model specifications (e.g., Flat tube/NACA 0014 tube geometry vs. circular tube), which would affect the performance of the heat transfer taking place, causing differences in the temperature distribution. Also, there are potential differences in the coolant properties as the oil coolant grade was not specified in the reference paper.

4.2.2. Conclusion From Comparisons

After the data has been compared with the numerical results, it is concluded that the results calculated numerically generally follow the distributions from the validation sources, albeit with some moderately large deviations in certain places. These deviations likely stemmed from the differences in assumptions made between the data and the numerical model, as well as the slight differences in some of the model specifications. Another potential source of discrepancy is the methodology used in the sources compared to the numerical. As the numerical model is based on theoretical computation, the sources derive their results through a combination of theory and experimental data. In addition, there are some areas where they used a higher fidelity of the components of the duct, such as taking into account the shape and efficiency of the diffuser/nozzle as well as the shaping of the heat exchanger fins (Flat tube/NACA 0014 tube geometry instead of simple circular tubes).

The observed differences between numerical findings and validation sources highlight the difficulty of reconciling theoretical computations with practical observations. A full sensitivity analysis will need to be performed to highlight these disparities further, methodically altering the parameters and assumptions inside the numerical model. The goal would be to determine the particular influence of each variable component on the findings, providing a better understanding of the disparities discovered. Furthermore, collaborative efforts with experimentalists should be pursued in the future to validate the numerical results through real-world experimentation. This joint approach, which combines theoretical simulations with empirical validation, has the potential to bridge the gap between numerical calculations and experimental data, resulting in a more resilient and accurate representation of the researched system.

5
Analysis of The Cooling Duct Subsystem

This chapter discusses the results obtained from testing the numerical models described in chapter 3.

5.1. Optimisation Of The Cooling Duct

This section discusses the results of the optimisation process defined in chapter 3.

5.1.1. Optimisation Convergence

The cause of termination of this optimisation process is because a feasible point of the objective value has been found, with the first-order optimality measure and the constraint violation is less than their tolerance. This means the optimisation process was successful with the given tolerances (as shown below) and that an optimal design was found. However, improvements can be made to the optimisation tool that will produce an improved design to the one obtained which will be discussed in detail in section 5.1.2. When optimising a function in MATLAB with the fmincon function, it is critical to watch the convergence history to confirm that the optimisation method is running properly. The convergence history of the objective function, design vector, constraint violations, and first-order optimality can be seen in figure 5.1:

It is observed that the objective function decreased, which is beneficial to the goal of this project. It is also noted that the first-order optimality and max constraint violation were increased initially (iterations 1-3), suggesting that the duct design exceeded the mass constraint, making it an infeasible design point. However, it then reduced with each iteration up to the order of 10e-4 and 10e-12, respectively, suggesting that the optimiser was correctly evaluating the problem and finding design points closer to the optimum values.

5.1.2. Optimisation Results

To optimise the duct size, the heat transfer that occurs must be fixed, which for this project is set at 1 MW. Furthermore, the optimisation procedure is repeated throughout the full flight profile to determine which phase necessitates the biggest duct sizing. When the optimisation method was run for each flight phase, it was discovered that the take-off phase yielded the greatest duct sizing. The following values were discovered as a result of this optimisation process:

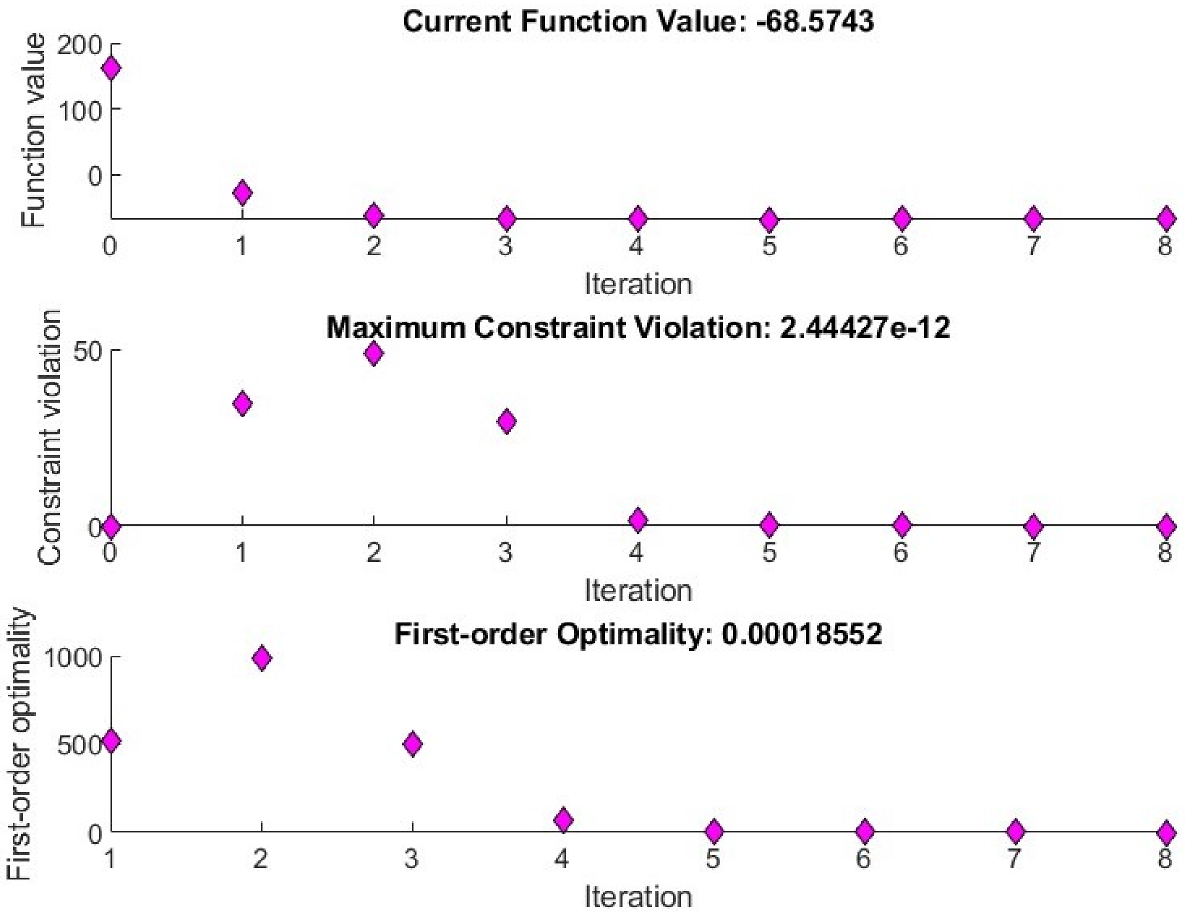

Figure 5.1: Convergence history of the cooling duct optimisation process

Table 5.1: Comparison of initial and final results of the optimisation process

Variable	Unit	Initial Value	Final Value
x	$[-]$	[1, 38.5126, 38.5126]	[1.0549, 0.1961, 0.2071]
f	$[N]$	160.76	-68.57
A_1	$[m^2]$	0.5556	0.336
A_2, A_3	$[m^2]$	1	1.7134
A_4	$[m^2]$	0.5556	0.3549
W_{HX}	$[m]$	1	1.309
L_{HX}	$[m]$	1	1.240
H_{HX}	$[m]$	1	1.309

With this table, the duct planform of the initial and final iterations can be shown in figure 5.2:

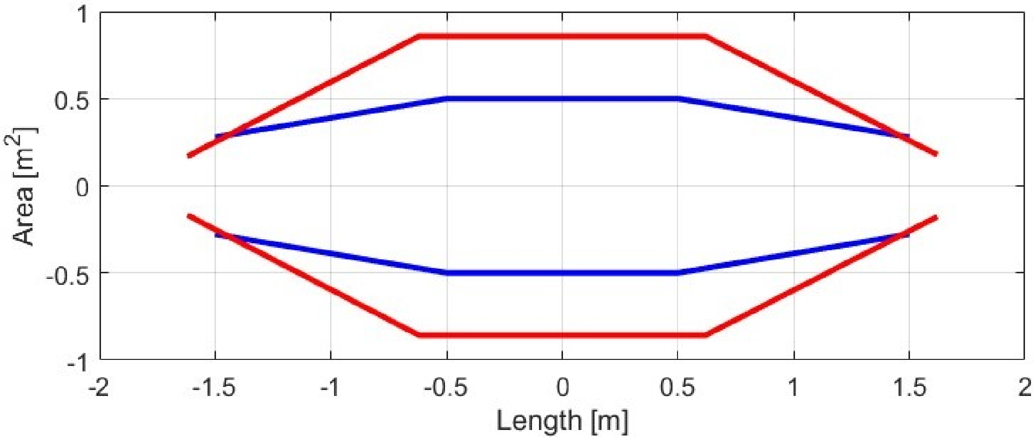

Figure 5.2: Comparison of the initial and final platform of the cooling duct

Where the blue planform is the initial duct, and the red planform is the final duct design. Comparing the initial and final iterations of this process, it can be seen that the drag decreased to a negative value, leading to a positive thrust. This suggests that the new duct design performs better in terms of aerodynamics and performance. The diffuser inlet and nozzle outlet areas have decreased, which has led to larger expansion and contraction effects, respectively, on the internal flow. In addition, the dimensions of the heat exchanger increased, which means a larger surface area is available for heat exchange to occur. A larger surface area leads to more contact between the hot and cold fluids, which leads to a larger heat transfer between the heat generated by the aircraft and the ambient air.

The duct's interior properties can be evaluated using the final design vector of the optimisation process, as illustrated in figure 5.3:

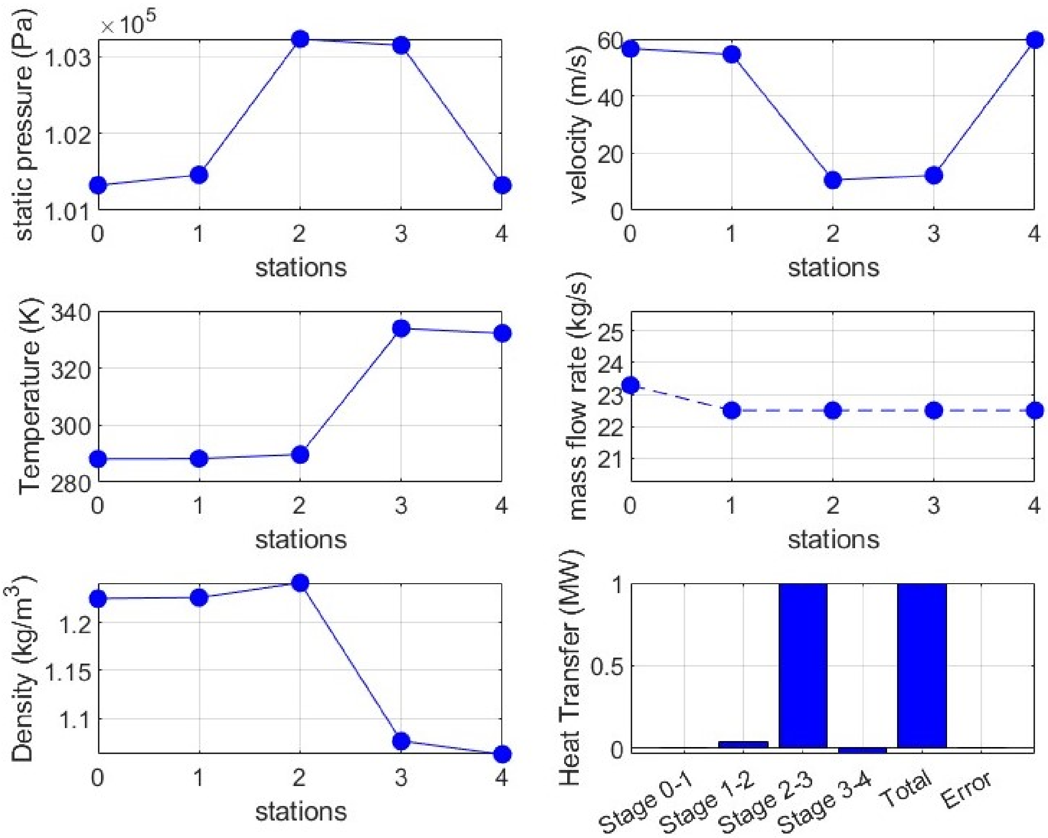

Figure 5.3: Internal properties of the final duct design

Looking at stages 1-2 on the pressure and velocity plot, it is observed that the diffuser effectively raises the pressure of ambient air while decreasing its speed. In addition, the same but opposite effect is seen at stages 3–4, as the nozzle effectively increases the velocity at the exit while reducing the pressure to the same level as the ambient air. This went in line with the more narrow designs of the diffuser and nozzle, which increased the effect of expansion and compression on the air, respectively.

The reduction of speed at the diffuser exit also improved the reduction in pressure loss on the heat exchanger, as observed on the pressure plot at stages 2–3, which would eventually lead to a lower radiator drag. The heat exchanger itself also seems to be quite efficient in terms of heat transfer due to the large temperature rise at stages 2–3 on the temperature plot.

Looking at the mass flow plot, it is observed that the core mass flow is conserved and only a small amount of mass flow was lost ($\approx$ 0.8 kg/s) when entering the duct. This implies that the duct is handling the incoming mass of air effectively. Also, looking at the heat transfer plots, it can be seen that the sum of the component heat transfers is equal to the heat transfer of the complete system (i.e., the error bar is empty) which suggests that the heat transfer is conserved as well.

5.2. Internal Analysis Of The Cooling Duct

This section investigates the flight profile analysis of the Dash 8-300 to see how the aircraft performs with the optimised duct in each flight phase. Using the standard flight profile of the Dash 8-300 in figure 3.9, the performance of the aircraft can be determined. The variables that are to be calculated are:

- Flight conditions (i.e. altitude, air speed, aircraft speed)
- Performance conditions (i.e. available power, net force, mass flow)
- Thermal conditions (i.e. Heat transfer)

Knowing the available power for each flight phase is one of the most critical pieces of information for designing the propulsion system as this will determine the sizing of the engines and the components within. From literature, the engine ratings of the Dash 8-300 are shown in table 5.2:

Table 5.2: Engine Ratings of the Dash 8-300, obtained from aircraft data [23]

Flight Phase	Power Rating [SHP]	Percentage [%]
Take-off	2380	100
Max continuous	2150	90.3
Max climb	2088	87.7
Max cruise	2030	85.3
Descent	1190	50
Landing	952	40

It was determined that the power rating for take-off and initial climb is constant at full power (i.e., 1860 kW), and the other climb phases are constant at max climb power (1631.8 kW). Using the methodology described in chapter 3, the duct properties for each flight phase can be seen in figure 5.4:

From this figure, it can be seen that the general profile matches that of the profile depicted in figure 5.3. When comparing each flight phase with their respective inputs, they align with what is expected, as these changes should only translate the profiles in the y direction based on their altitude and flight velocity. What is more interesting to observe are the outputs of the duct for the flight profile, as shown in figure 5.5:

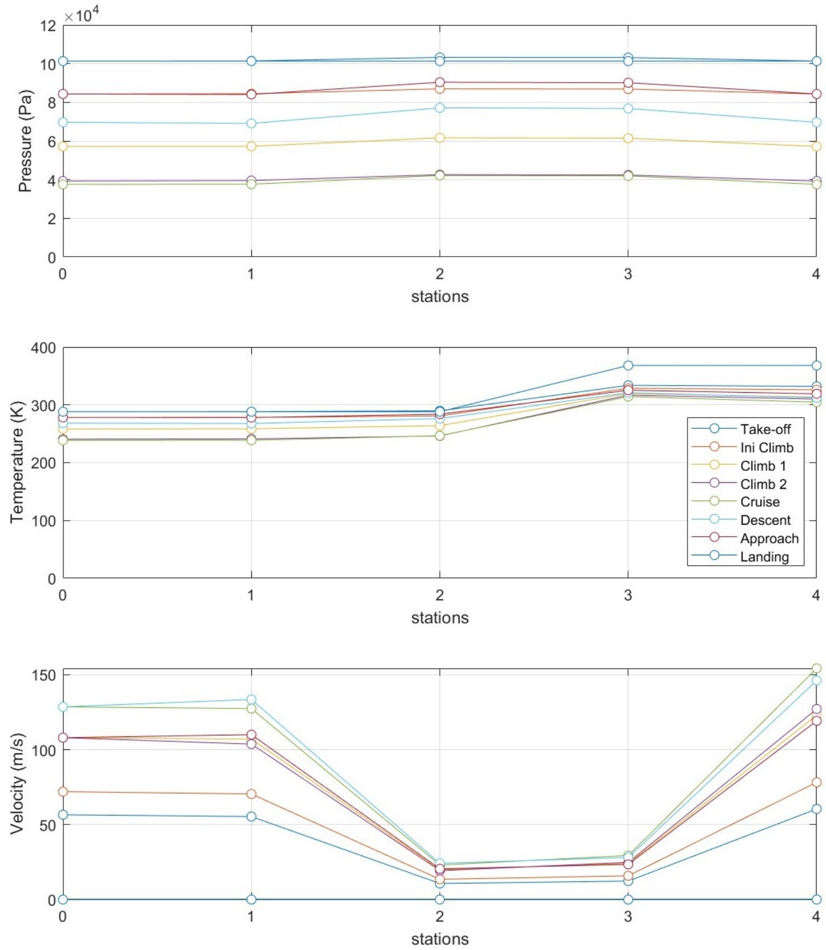

Figure 5.4: Duct properties for each flight phase using the optimised cooling duct

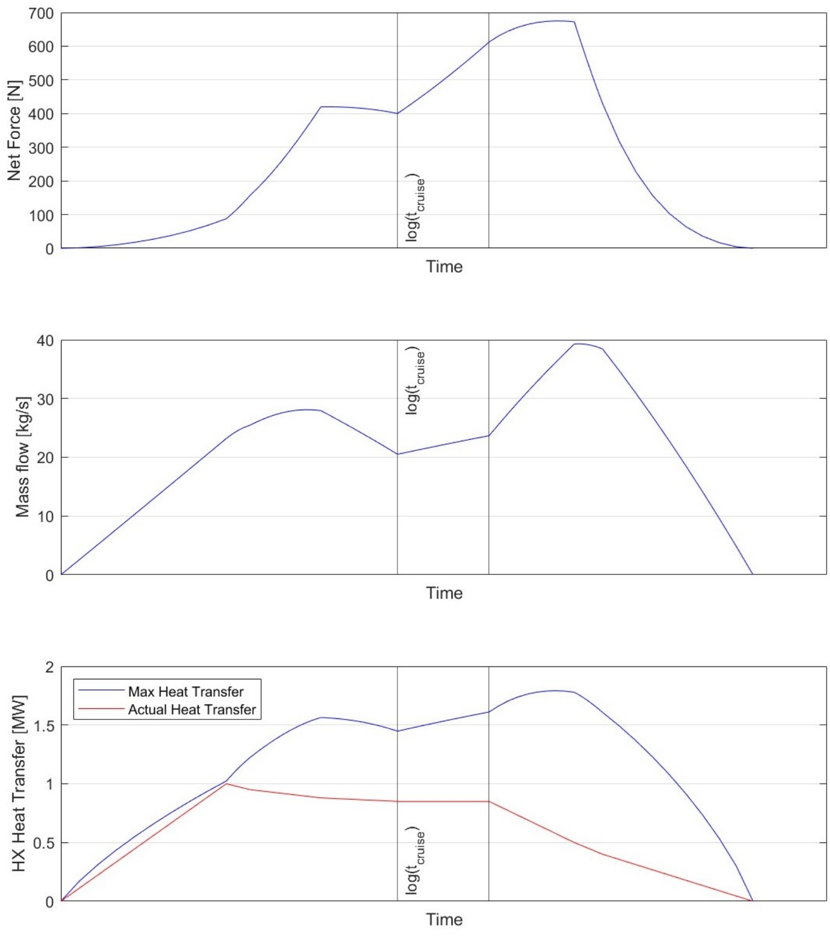

Figure 5.5: Duct outputs for each flight phase using the optimised cooling duct

The dark vertical borders, which depict the cruise phase, are the first thing to notice. Because the other flying phases are so small in contrast, the logarithm of the time in cruise is used to monitor them more precisely.

The values of net force and mass flow generally increase up to the approach phase, with a slight decrease in the second climb phase, possibly due to the slower rate of ascent. Furthermore, it is noticed that these values continue to rise during the descending phase. This is logical given that the flight velocity has not dropped since the cruise phase, resulting in larger net force and mass flow numbers.

Finally, two configurations may be observed in the heat transfer plot. The first is the maximal heat transfer output that the optimal duct can form. The other plot depicts the reality plot, as the optimisation method was designed to maximise heat transfer output during take-off. This demonstrates that the optimised duct might be a disadvantage in terms of weight and drag during later flight phases since it is not as vital to utilise as it is at the start of the flight.

5.3. Preliminary External Analysis Of The Cooling Duct

Using the methodology described in chapter 3, an initial evaluation of the duct was simulated using CFD. This evaluation was made in cruise conditions to observe how well the duct performs throughout the majority of the flight. From observing the simulations, it can be seen that the generated mesh meets the quality criteria and the solution is converged. The mesh analysed contained 30420 uniform elements. This was done to represent the variation of the flow properties accurately. These flow properties can be seen in figure 5.6:

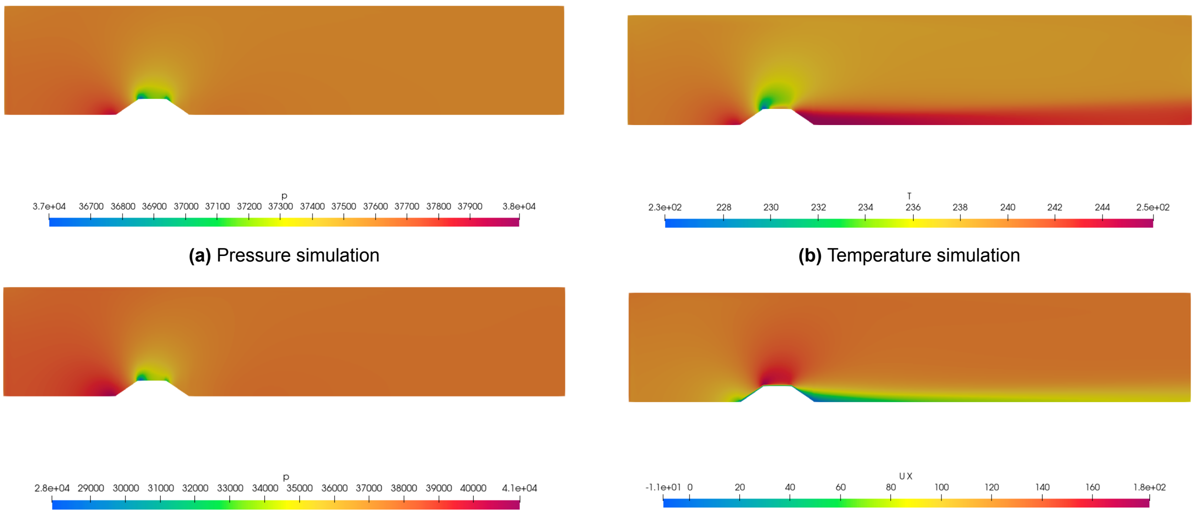

(a) Pressure simulation

(b) Temperature simulation

(c) Density simulation

(d) Velocity simulation

Figure 5.6: CFD simulations of the top wall of the optimised cooling duct using ParaView

The pressure simulation shows that the region around the diffuser intake is greater than the free stream, indicating a probable separation point. Furthermore, the wall above the heat exchanger has low-pressure areas, which might cause potential drag.

Similarly, the temperature profile exhibits high temperatures at the diffuser input and low temperatures near the heat exchanger wall. There is also a noticeable temperature rise at the nozzle wall, which dissipates into the surrounding air. This zone might be caused by boundary layer effects, adiabatic compression when the pressure region from the heat exchanger wall to the nozzle wall rises, or both.

In the velocity profile, low-speed zones are identified at the diffuser wall, while high-speed regions are recognised at the heat exchanger. Furthermore, there is a broad region beyond the nozzle wall with low speed, which normalises farther upstream. The nozzle wall is most likely impeding the free-stream air as it passes around the duct.

From these CFD simulations, the aerodynamic forces acting on the duct walls were recorded. The convergence of the drag force can be seen in figure 5.7:

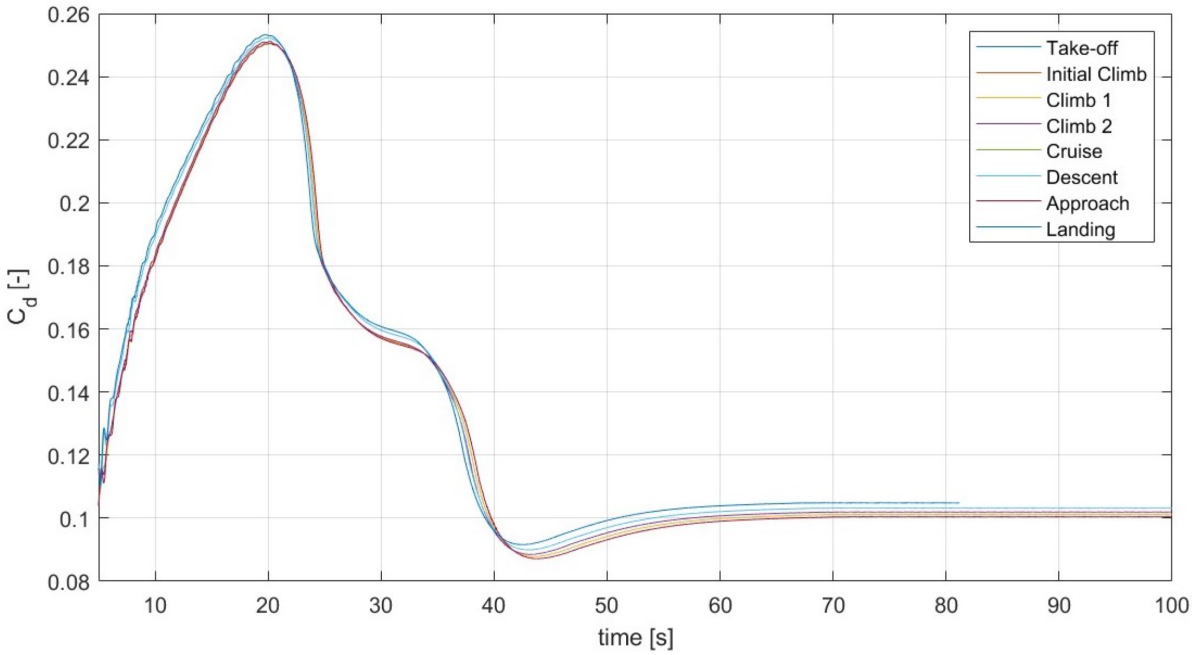

Figure 5.7: Convergence of aerodynamic forces of the top wall of the optimised cooling duct obtained from the CFD simulation

Assuming that the lower part of the duct would produce the same values, the total drag force acting on the external walls of the duct is presented in table 5.3:

Table 5.3: Total external drag forces of the optimised cooling duct

Flight Phase	C_D
Take-off	0.2006
Initial climb	0.2024
Climb 1	0.2024
Climb 2	0.2039
Cruise	0.2096
Descent	0.2064
Approach	0.2009
Landing	0.2006

6 Analysis At The Aircraft System Level

This chapter discusses the results obtained from testing the effects of the numerical models on the aircraft described in section 3.5.

6.1. Payload-Range Analysis Of The Aircraft System

With the internal and external properties established, it is now possible to construct the payload-range diagram and compare them based on the following configurations:

- Configuration 1: Reduced fuel weight, constant payload weight
- Configuration 2: Reduced payload weight, constant fuel weight
- Configuration 3: Reduced fuel and payload weight (50:50 mixture)

How these configurations affect the methodology of constructing the payload-range diagrams is discussed in sections 6.1.1 to 6.1.3.

6.1.1. Configuration 1

For configuration 1, the weight of the ducts is deducted from the fuel weight. This will modify equation (3.88):

$$W_f = \begin{cases} (MTOW - OEW_{FC} - W_{p,max} - 2 \cdot W_{duct}) \cdot (1 - f_{reserve}) & \text{Point B} \\ (W_{f,max} - 2 \cdot W_{duct}) \cdot (1 - f_{reserve}) & \text{Point C \& D} \end{cases} \tag{6.1}$$

And equation (3.89):

$$W_{diff} = MTOW - OEW_{FC} - W_f - W_{f,reserve} - W_{p,pax} - 2 \cdot W_{duct} \tag{6.2}$$

6.1.2. Configuration 2

For configuration 2, the weight of the ducts is deducted from the payload weight. This will modify equation (3.86):

$$W_p = W_{p,pax} - 2 \cdot W_{duct} \tag{6.3}$$

Equation (3.89) is also modified to:

$$W_{diff} = MTOW - OEW_{FC} - W_f - W_{f,reserve} - W_p - 2 \cdot W_{duct} \tag{6.4}$$

6.1.3. Configuration 3

For the third and final configuration, the weight of the ducts is equally deducted from the fuel weight and payload weight. The modified equations are:

$$W_f = \begin{cases} (MTOW - OEW_{FC} - W_{p,max} - W_{duct}) \cdot (1 - f_{reserve}) & \text{Point B} \\ (W_{f,max} - W_{duct}) \cdot (1 - f_{reserve}) & \text{Point C \& D} \end{cases} \tag{6.5}$$

$$W_p = W_{p,pax} - W_{duct} \tag{6.6}$$

Equation (6.4) is also used for this configuration.

6.1.4. Results

These payload-range estimates will also be compared to the conventional results of the Dash 8-300. These configurations can be seen in figure 6.1:

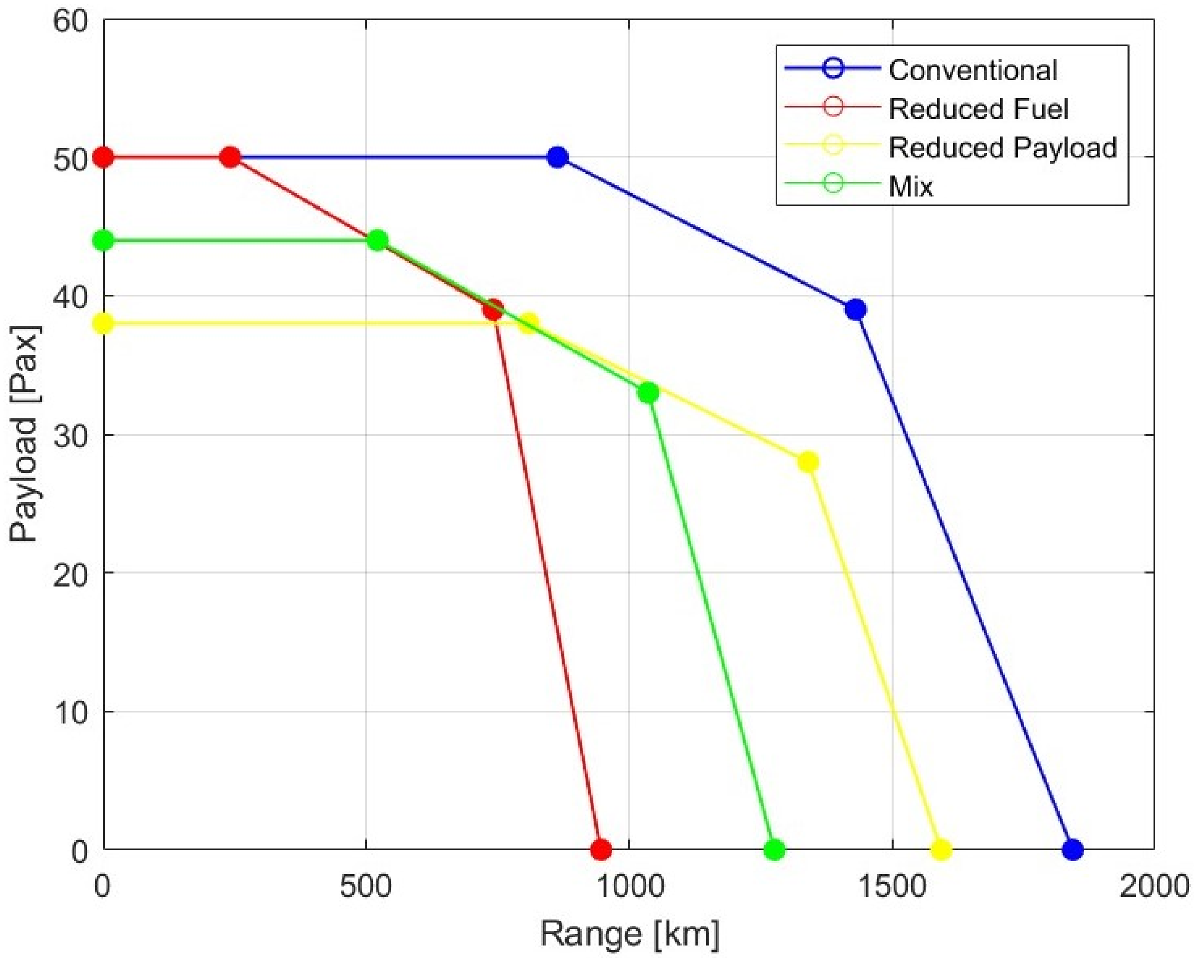

Figure 6.1: Payload-Range diagram comparison of the Dash 8-300 cooling duct configurations

The reduced fuel configuration significantly reduced the aircraft's range (48.6%), whereas the reduced payload configuration kept the majority of the performance features (13.6% loss). In the case of the decreased payload configuration, however, the number of passengers was cut from 50 to 38 (a 24% reduction). As a result, depending on the mission, the decreased fuel arrangement may be more advantageous as it still transports the full 50 people despite the reduced range.

Another option is to lower both the fuel and cargo weight equally to alleviate their respective drawbacks. Figure 6.1 shows that the range improved considerably when compared to the decreased fuel design (30.8%) while keeping a greater number of passengers (44) than the reduced payload option. With a 17.8% better range and a 12% retention in passenger space compared to the lower fuel and payload configurations, respectively, this configuration may be beneficial in a wide range of flight missions.

Note that these calculations are subject to change as it was assumed that the power specifications are the same when switching the Dash 8-300 propulsion system from the conventional kerosene system to the fuel cell system.

6.2. Performance Diagrams of the Aircraft System

When considering the duct configuration, there are no changes for the stall and landing phases since the addition of the ducts does not affect these values based on the assumptions made in section 3.5. However, in reality, the changes in the propulsion system and the fuel used would affect the weight ratios in stall and landing, so it is worth taking a second look in the future when this project progresses further.

The aircraft's take-off phase relies on the amount of power it generates. Hence, the extra force generated by the duct is included in the calculation:

$$\left(\frac{P}{W}\right)_{TO,new} = \frac{1}{W_{TO}}\left[W_{TO}\cdot\left(\frac{P}{W}\right)_{TO} + (F_{net,TO}\cdot V_{TO})\right] \tag{6.7}$$

The same can be said for the cruise phase:

$$\left(\frac{P}{W}\right)_{cr,new} = \frac{1}{W_{cr}}\left[W_{cr}\cdot\left(\frac{P}{W}\right)_{cr} + (F_{net,cr}\cdot V_{cr})\right] \tag{6.8}$$

With these additions and the performance properties found for the conventional configuration, the power loading and wing loading of the aircraft system can be plotted:

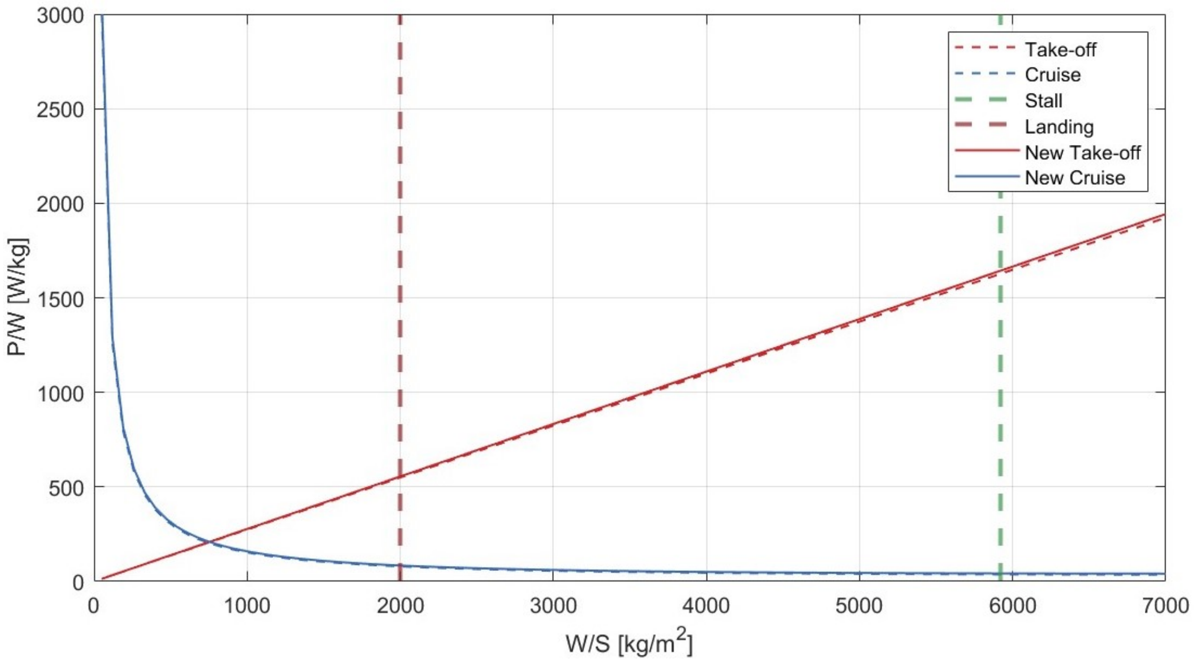

Figure 6.2: Power loading and wing loading of the Dash 8-300 cooling duct configuration

From these curves, it is observed that the addition of the ducts does improve the power loading and wing loading relationship for the take-off and cruise phases, albeit by a small margin (0.0133% and 0.0759%, respectively). While the percentage increase may appear insignificant, even minor improvements in power loading and wing loading can result in significant benefits in terms of performance, fuel efficiency, and mission flexibility. This small gain may be significant during specific flight phases or under certain operational conditions, demonstrating the ability of cooling ducts to contribute to the optimisation of the aircraft's aerodynamic characteristics. In the future, this knowledge can be utilised to fine-tune and personalise the integration of cooling ducts into electric aircraft, considering specific mission requirements and operating scenarios, to maximise the system's performance.

After analysing the performance diagram, it is required to compare the propulsive conditions of the conventional aircraft to the cooling duct configuration. By evaluating these characteristics, one can determine the effect of the cooling ducts on the aircraft's total fuel economy. The conventional design provides a baseline, and any observed differences in fuel usage and consumption in the cooling duct configuration will provide insight into the effectiveness of this subsystem in improving the aircraft's operational and environmental performance.

The maximum fuel weight for each configuration is determined based on the configurations described in the construction of the payload-range diagram (section 6.1):

$$W_{f,max,c1} = W_{f,max} - (W_{duct} + W_{gl}) \tag{6.9}$$

$$W_{f,max,c2} = W_{f,max} \tag{6.10}$$

$$W_{f,max,c3} = W_f, max - 0.5 \cdot (W_{duct} + W_{gl}) \tag{6.11}$$

For the fuel weight used per phase, the following equation is used for each configuration:

$$W_{f,ci} = W_{f,max,ci} - (MTOW - W_{i-1} \cdot f_i) \tag{6.12}$$

$$\tag{6.13}$$

With the fuel usage determined, the fuel flow can be calculated for each configuration using the following equation:

$$\dot{m}_{f,i} = \frac{W_{f,i}}{t_i} \tag{6.14}$$

Lastly, the specific fuel consumption for each configuration is computed:

$$SFC_i = \frac{\dot{m}_{f,i}}{T_{AC,i} + F_{net,i}} \tag{6.15}$$

With these properties determined, the distribution of these properties across the flight profile can be plotted in figure 6.3:

The figure shows that the integration of cooling ducts results in a reduction in fuel usage, fuel flow, and specific fuel consumption (SFC), indicating considerable improvements in the fuel efficiency of the aircraft's propulsion systems. Configuration 1 had the largest effect on these properties as the complete duct mass and the glycol weight were deducted from the maximum fuel weight, which led to a much lower fuel flow and SFC. The second configuration had the same effect, although it was more muted compared to configuration 1, as only half of the duct and glycol weight is considered (with the other half being deducted from the payload). Configuration 2 did not have any changes in the fuel usage or fuel flow as the duct was deducted completely from the payload. However, as the thrust of the duct was taken into account, the specific fuel consumption did decrease compared to the conventional aircraft system.

Overall, the addition of cooling ducts results in a reduction in the quantity of fuel used for a given level of thrust, reducing operational costs and increasing the aircraft's economic viability and environmental sustainability. Furthermore, the observed reduction in specific fuel consumption suggests that the aircraft can travel longer distances per unit of fuel, increasing its total range/endurance capability. However, considering the reduction in fuel weight, it would also suggest that the range would decrease, so further research is required to ensure that the benefits of the cooling ducts outweigh the drawbacks of fuel reduction.

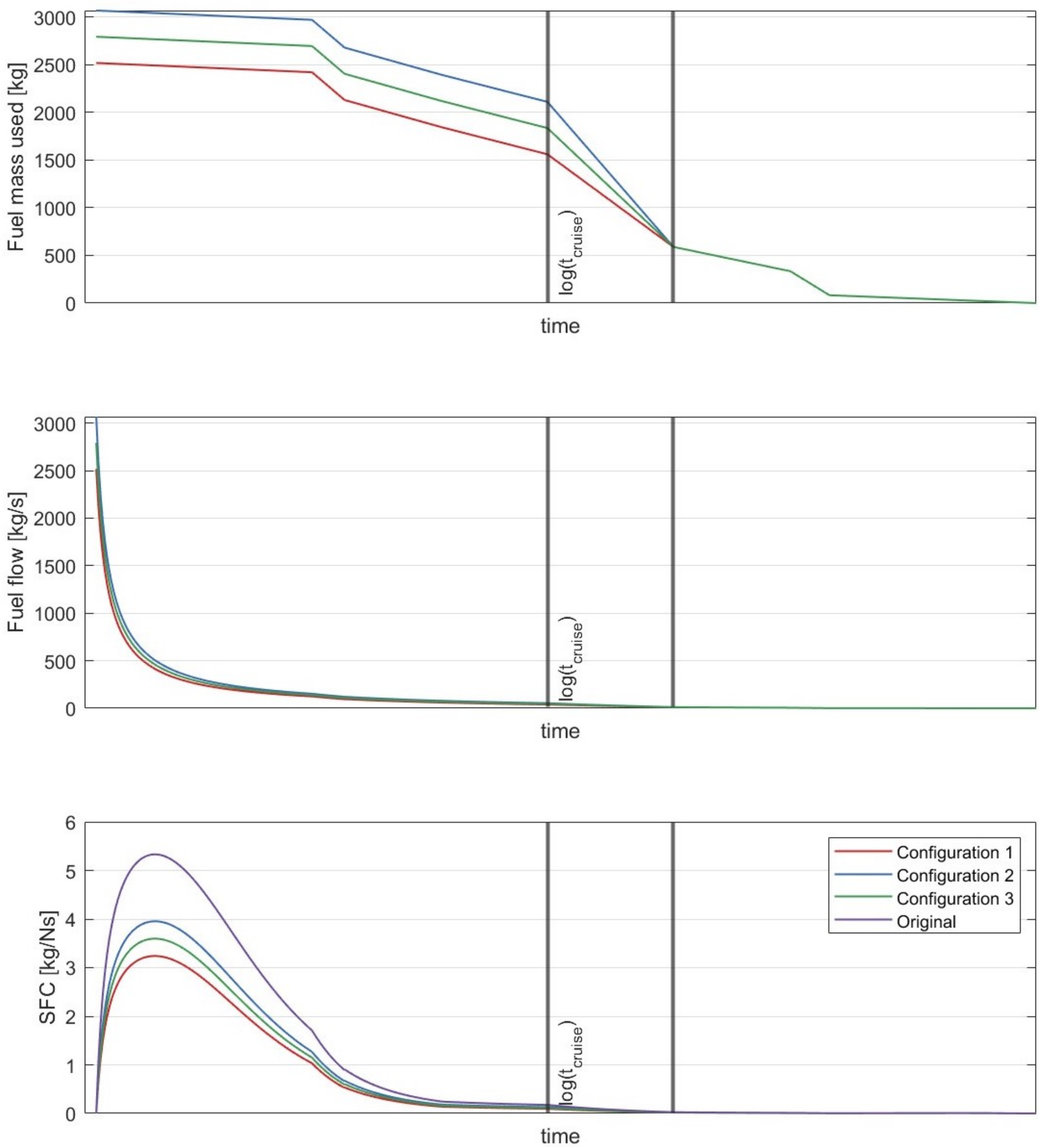

Figure 6.3: Propulsive properties of the Dash 8-300 cooling duct configurations

7 Conclusion & Recommendations

The definitive results and insights obtained from the comprehensive research and analysis undertaken throughout this technical study are provided in this chapter, which summarises key findings and recommendations.

7.1. Conclusion

The comparison between the numerical results and the validation sources has provided valuable insights into the accuracy of the numerical model. While the numerical results generally align with the distributions of the validation sources, certain discrepancies were observed. These discrepancies can be attributed to divergent assumptions between the data and the numerical model, as well as variances in specific model specifications. Moreover, differences in methodology emerged as a notable factor; the numerical model relied on theoretical computations, whereas the sources combined theory with experimental data. Additionally, variations in component fidelity, such as the detailed consideration of duct components like diffusers, nozzles, and heat exchanger fins, contributed to the observed differences. Recognising these distinctions is crucial for refining the numerical model and advancing our understanding of the studied system, emphasising the importance of reconciling theoretical computations with experimental observations for comprehensive and accurate analyses in future research endeavours.

Comparing the iterated duct variables and the original design, it can be seen that the optimisation process did converge towards an optimum design. The diffuser inlet and nozzle outlet are more narrow, resulting in increased expansion and contraction effects internally. Additionally, the heat exchanger dimensions were enlarged, facilitating more substantial heat exchange due to increased contact between hot and cold fluids. However, this output could have improved when taking certain factors into account when setting up the optimiser. One such factor is to introduce additional disciplines, mainly structures and performance. These disciplines were not initially introduced as they are concerned with the aircraft as a whole, whereas the scope of this optimisation process is solely on the duct. This approach takes into account how the duct interacts with the entire system, resulting in improved overall performance and efficiency. This is required as aircraft components are interrelated, and modifications to one might have an impact on others. Another factor is to increase the fidelity of the diffuser and nozzle design, as their current scheme is quite simplified. To begin with, the diffuser and nozzle are just straightforward divergent and convergent cones, respectively. These components' forms can be changed to maximise their impact on ambient air flow and lessen the negative effects of pressure loss and drag.

The research of various aircraft configurations, such as decreased fuel, payload, and a balanced approach, gives useful information for optimising the Dash 8-300's performance. According to the analysis, the lower fuel arrangement drastically limited the aircraft's range by 48.6%. The decreased cargo option, on the other hand, suffered a very little performance loss (13.6%) despite admitting 38 people, a 24% reduction from the usual capacity. When both fuel and cargo weights were reduced at the same time, a compelling alternative arose, overcoming the limitations associated with separate reductions.

When compared to the reduced fuel design, this balanced strategy increased the range by 30.8%. Surprisingly, it could also transport 44 persons, reserving 88% of the usual passenger capacity. This configuration offers a viable alternative for a wide range of flight missions and scenarios, with a 17.8% increase in range and 12% greater passenger room than the lower fuel and payload configurations, respectively. It is important to note, however, that these estimates are predicated on constant power specs, assuming a changeover from the standard kerosene system to the fuel cell system in the Dash 8-300. Additional refining and real-world testing are required to confirm these findings and fully exploit the potential of these arrangements.

This in-depth examination has shed light on the complex interaction of numerous elements inside the system. It is clear that pressure, temperature, flight velocity, and nozzle output area jointly dominate the dynamics, with a range of around 8-12% impacting mass flow and 11-41% impacting net force. The influence of the diffuser area and heat exchanger size, on the other hand, is insignificant, ranging from 0-1%. When it comes to heat transmission and heat exchanger effectiveness, temperature emerges as the primary actor, with a significant differential of around 32-64%. Furthermore, the heat exchanger dimensions and nozzle output area continue to exert notable effects, ranging from 0.08-0.13% for heat transfer and 8-12% for heat exchanger effectiveness.

7.2. Recommendation

This section presents the recommendations of this project for future development of the cooling duct subsystem.

7.2.1. Validation, & Sensitivity Analysis

Moving forward, it is imperative to conduct a detailed analysis to pinpoint the exact factors responsible for the observed discrepancies. This could involve a systematic review of the assumptions, model specifications, and methodologies employed in numerical simulations and the validation sources. Additionally, further investigations might delve into the impact of the varying fidelity levels of components, exploring how the intricacies of diffusers, nozzles, and heat exchangers affect the overall system behaviour.

However, since this is a novel idea for an electric aircraft, there is not much prior literature with test data to compare, making it challenging to gather. By building models to evaluate and contrast their outcomes with those of the numerical tool, test data can be collected through experimentation.

Furthermore, a more comprehensive sensitivity analysis could be carried out to quantify the influence of each differing parameter and assumption on the final results. In-depth sensitivity studies would not only enhance the understanding of the system's response to different variables but also aid in prioritising which aspects require closer scrutiny and potential adjustments.

Moreover, considering the practical applications of this study, it might be valuable to explore the potential implications of these discrepancies in real-world scenarios. Understanding how these variations affect the system's performance under specific conditions or in different environments could provide valuable insights for engineering applications.

7.2.2. Numerical Model & CFD Model

In terms of the numerical model, incorporating it into the aircraft system, particularly investigating the areas of structure and performance, is a critical issue. Initially, the aircraft was not considered since the major focus of this evaluation was on the duct itself. Adopting this larger viewpoint provides a thorough knowledge of how the duct interacts with the overall aircraft system. Recognising the interconnection of multiple aircraft components is critical since changes made in one area can have an impact on the entire system's overall operation. An example is the optimisation of the duct, which produced a narrow inlet and outlet and a large heat exchanger. Although these properties do lead to improved heat transfer, care must be taken to ensure that the dimension changes are not too extreme. Excessively narrow passages can lead to flow restriction, causing an increased pressure drop and a reduced airflow rate. Also, a larger heat exchanger would lead to a larger payload for the aircraft to carry, affecting its propulsive and performance properties. Therefore, it is necessary to find an optimal balance between flow efficiency and heat transfer effectiveness to maximise the performance of the system.

In addition, it is also critical to improve the design of the duct components, particularly the diffuser and nozzle. Their design requires higher fidelity to improve their functions and can have a substantial impact on the flow of ambient air, reducing negative consequences such as pressure loss and drag. This more complex analysis promises to improve the aircraft system's overall efficiency and performance.

The CFD model only provided a preliminary assessment of the top duct wall. This is not an ideal choice since it does not imitate the flow of the entire duct. The first step in improving this is to replicate the entire duct, with flow travelling both inside and outside. There are issues with this since OpenFoam does not create internal faces, making it impossible to evaluate the internal changes of the heat exchanger or represent an empty duct while examining the duct's outward impacts. As a result, alternate ways to replicate this in OpenFoam must be investigated, as well as other CFD programs that do not have these constraints.

7.2.3. Comparison To Alternative Solutions

In addition to improving the numerical model, it would be beneficial to investigate alternative solutions and compare them to ducted radiators to determine if this solution is the best.

An alternative concept to ducted radiators is aircraft surface heat exchangers. As the heat transfer that takes place between the skin and ambient air requires no extra parts or cut-outs like the inlet ducts, this alternative may be more advantageous in decreasing the drag and weight penalty [9, 29]. The interaction between the aircraft and the boundary layer [9, 29] would be impacted by this heat transfer at the surface, perhaps resulting in an even greater reduction in drag. However, further research is necessary, especially when examining the variations in how laminar and turbulent flows interact. The structural limitations must also be considered, as this system is more substantial and intricate than the ducted radiator system.

Focusing on the coolant used to transport the heat exchanger absorbed from the system was another approach that was taken into consideration. Liquid cooling could be used as an alternative to air cooling. The two methods of liquid cooling are warm (defined as at or above room temperature) and cryogenic (defined as temperatures mostly below 0 degrees Celsius).

Warm liquid cooling is preferable to air cooling since it doesn't require ventilation and typically has better heat transfer coefficients, which means it absorbs heat more quickly. However, liquid cooling demands pumps to move the coolant throughout the system and store the coolant, which raises the bulk and power needs. Cryogenic cooling, on the other hand, gives engineers the chance to superconduct electrical parts, increasing their efficiencies and power densities [9]. However, choosing this alternative would result in higher bulk and power demands, which would offset the benefits of this design choice. This problem could be resolved by cooling these components using liquid hydrogen before combustion [9]. However, this method has its disadvantages, as it calls for more infrastructure and safety precautions. Furthermore, this architecture is not appropriate for systems that cannot or do not use hydrogen as a fuel.

References

[1] F.W. Meredith. *Cooling of aircraft engines with special references to ethylene glycol radiators enclosed in ducts*. Tech. rep. ARC, Reports and Memoranda No. 1683, 1935.

[2] J. Leland Atwood. *Origin and Evolution of the Mustang*. Tech. rep. Air Power History, 1993.

[3] H. Winter. *Contribution to the theory of the heated duct radiator*. Tech. rep. NACA, Technical Memorandums Vol. 15, No. 10/11, 1938.

[4] A. Silverstein. *Experiments on the recovery of waste heat*. Tech. rep. NACA, Special Report No. 111, 1939.

[5] P. Bertles. *De Havilland Mosquito: The Original Multirole Combat Aircraft*. Fonthill Media, 2015.

[6] R. Jackson. *Messerschmitt Bf 109 A-D Series*. Osprey Publishing, 2015.

[7] L. Piancastelli and M. Pellegrini. *The bonus of aircraft piston engines, an update of the Meredith effect*. Tech. rep. International Journal of Heat and Technology, 2007.

[8] L. Piancastelli, L. Frizziero, and G. Donicci. *The Meredith Ramjet: An efficient way to recover the heat wasted in piston engine cooling*. Tech. rep. ARPN Journal of Engineering and Applied Sciences, 2015.

[9] J. Freeman et al. *Challenges and opportunities for electric aircraft thermal management*. Tech. rep. Empirical Systems Aerospace, Inc., 2014.

[10] T. A Talay. *Introduction to the Aerodynamics of Flight*. Tech. rep. National Aeronautics and Space Administration, 1975.

[11] J. Anderson. *Fundamentals of Aerodynamics (SI units)*. McGraw hill, 2011.

[12] R. K. Shah and D. P. Sekulic. *Fundamentals of Heat Exchanger Design*. John Wiley and Sons, Inc., 2003.

[13] R. K. Shah and W. W. Focke. *Plate Heat Exchangers and their Design Theory in Heat Transfer Equipment Design*. R. K, 1988, pp. 227–254.

[14] H. Peng and X. Ling. *Optimal design approach for the plate-fin heat exchangers using neural networks cooperated with genetic algorithms*. School of Mechanical and Power Engineering, Nanjing University of Technology, China, 2007.

[15] R. M. Manglik and A. E. Bergles. “Heat Transfer and Pressure drop Correlations for the Rectangular Offset-Strip-Fin Compact Heat Exchanger”. In: *Exp* 10 (1995), pp. 171–180.

[16] S. Kakac and H. Liu. *Heat Exchangers*. CRC Press, New York, 1998.

[17] Theodore L Bergman et al. *Incropera’s Principles of Heat and Mass Transfer*. Wiley Global Education, 2017.

[18] J.P. Holman. *Heat Transfer, 10th edition*. Mc-GrawHill Higher education, 2010.

[19] J.Lienhard V J. Lienhard IV. *A Heat Transfer Textbook, 5th edition*. Phlogiston Press, 2020.

[20] Kays, W. M., and A. L. London. *Compact Heat Exchangers*. McGraw-Hill, New York, 1984.

[21] T. Holzmann. *Mathematics, Numerics, Derivations and OpenFOAM(R), Holzmann CFD*. Vol. 10. URL www. holzmann-cfd. de, DOI:10.13140/RG.2.2.27193.36960.

[22] WinAir. *The Complete Guide to the Bombardier Dash 8 Aircraft*. Tech. rep. Win Air, 2020.

[23] Universal Airlines. *De Havilland - Dash-8-Q300*. `http://www.uvairlines.com/admin/fleetdownloading/uni-dash8.htm`.

[24] TU Delft. *Payload Range Diagrams*. `https://www.aerostudents.com/courses/aerospace-design-and-systems-engineering-elements-1/Pay%loadRangeDiagrams.pdf`. 2015.

[25] TU Delft. *Data and formulae for aircraft preliminary weight estimation and sizing*. https://www.aerostudents.com/courses/aerospace-design-and-systems-engineering-elements-1/DataAndFormulaSheet.pdf. 2015.

[26] drs. Z. Berdowski et al. *Survey on standard weights of passengers and baggage*. Tech. rep. EASA, 2009.

[27] UI. *Feasibility Study Hydrogen IQ*. Tech. rep. Technology Park Ypenburg, Laan van Ypenburg 108, 2497 GC Den Haag: Unified International, 2018.

[28] Pratt & Whitney. *PW100*. https://engineering.purdue.edu/~propulsi/propulsion/jets/tprops/pw100.html. 2022.

[29] H. Kellermann, A.L. Habermann, and M. Hornung. "Assessment of aircraft surface heat exchanger potential". In: *Aerospace* 7.1 (2019), p. 1.